Calibration of imperfect mathematical models by multiple sources of data with measurement bias

Mengyang Gu\*, Kyle Anderson\*\*, and Erika McPhillips \*

- \* Department of Statistics and Applied Probability, UC Santa Barbara
  - \*\* California Volcano Observatory, United States Geological Survey

#### Abstract

Model calibration involves using experimental or field data to estimate the unknown parameters of a mathematical model. This task is complicated by discrepancy between the model and reality, and by possible bias in the data. We consider model calibration in the presence of both model discrepancy and measurement bias using multiple sources of data. We apply our technique to the calibration of a geophysical model of Kīlauea Volcano, Hawai'i, using radar satellite interferograms. We compare the use of models calibrated using multiple data sets simultaneously with results obtained using aggregated data. We derive distributions for the MLE and Bayesian inference, both implemented in the RobustCalibration package available on CRAN. Analysis of both simulated and real data confirm that our approach can identify the measurement bias and model discrepancy using multiple sources of data, and provide better estimates of model parameters.

KEYWORDS: Data aggregation; Bayesian inference; prior; radar interferogram; identifiability; prediction.

#### 1 Introduction

Mathematical models are often used to describe various phenomena in science and engineering. To make a mathematical model useful, one often first needs to estimate the unobserved parameters in the model using experimental observations or field data – a process generally known as model calibration (or data inversion). As the mathematical model is almost always an imperfect representation of reality, recent work on model calibration has focused on inclusion of a discrepancy function which accounts for the difference between the mathematical model and physical reality. In Kennedy and O'Hagan (2001), the discrepancy function is modeled as a Gaussian stochastic process (GaSP), and in combination with the calibrated mathematical model often leads to more precise predictions of reality. However, variability in the data can be explained by the discrepancy function in this approach, which degrades the ability of the calibrated mathematical model to predict reality Arendt et al. (2012a). Recent studies based on  $L_2$  calibration (Tuo and Wu, 2015), LS calibration (Wong et al., 2017), orthogonal Gaussian stochastic processes (Plumlee, 2017), and scaled Gaussian stochastic processes (S-GaSP) (Gu and Wang, 2018), aim to solve the identifiability problem of calibrating model parameters while maintaining good predictive performance.

In this work, we focus on spatially correlated patterns of measurement error caused by the device or field conditions, which we term measurement bias. Though the discrepancy function is widely considered in calibration problems, measurement biases have not been well-studied, although they are reported in many previous studies (see e.g. (Zebker et al., 1997; Hooper et al., 2007)). The measurement bias can vary across different data sources (caused by device or environmental conditions), while the discrepancy function is invariant across different data sources. Simultaneous analysis of both measurement bias and model discrepancy has rarely been considered. In Oliver and Alfonzo (2018), both effects were considered, whereas the model discrepancy was defined as a linear trend of the predictors, which may be restrictive. Here we will introduce a new statistical method utilizing multiple sources of data to simultaneously model discrepancy, measurement bias, and noise.

We apply the new statistical methodology to calibrate geophysical models of satellite radar data. Over the last 25 years, satellite-based radar measurements have made it possible to map deformation over broad swathes of the Earth's surface to sub-centimeter accuracy from space, revolutionizing scientists' ability to record and model deformation of the Earth's surface (Massonnet et al., 1995; Bürgmann et al., 2000; Pinel et al., 2014; Biggs and Pritchard, 2017). Interferometric synthetic aperture radar (InSAR) interferograms are most often obtained using data from orbiting microwave-band radar satellites. By interfering two radar images of the surface taken from a satellite at different times, changes in radar phase record temporal changes in the position of the Earth's surface along the oblique line-of-sight (LoS) vector between satellite and ground. Because only fractional phase change can be measured directly (the number of complete phase cycles between the satellite and ground is not known), these images are wrapped by the radar's wavelength. Unwrapping an image by spatial integration of the phase gradient – relative to a point believed to be non-deforming – yields relative LoS deformation, in units of distance change (Chen and Zebker, 2001).

Despite these advances, however, the interpretation of InSAR data is often greatly complicated by noise and bias. After removing phase due to elevation of Earth's surface, the wrapped phase  $\phi$  for each pixel on the ground can be described by (e.g. Hooper et al., 2007)

$$\phi = W \left\{ \phi_d + \phi_a + \phi_o + \phi_l + \phi_n \right\}, \tag{1}$$

where W is a "wrapping" operator that drops full phase cycles,  $\phi_d$  is due to LoS ground displacement,  $\phi_a$  is propagation delay due to atmosphere conditions (Gong et al., 2016),  $\phi_o$  and  $\phi_l$  are phases due to satellite orbital error and look angle error, respectively, and  $\phi_n$  accounts for remaining noise (Hooper et al., 2007). The unwrapping procedure converts phase to ground displacements, which are typically modeled.

In this work we utilize data from Kīlauea Volcano, one of the most active volcanoes on the Island of Hawai'i, and erupted semi-continuously from 1983-2018. In 2018, a historically-

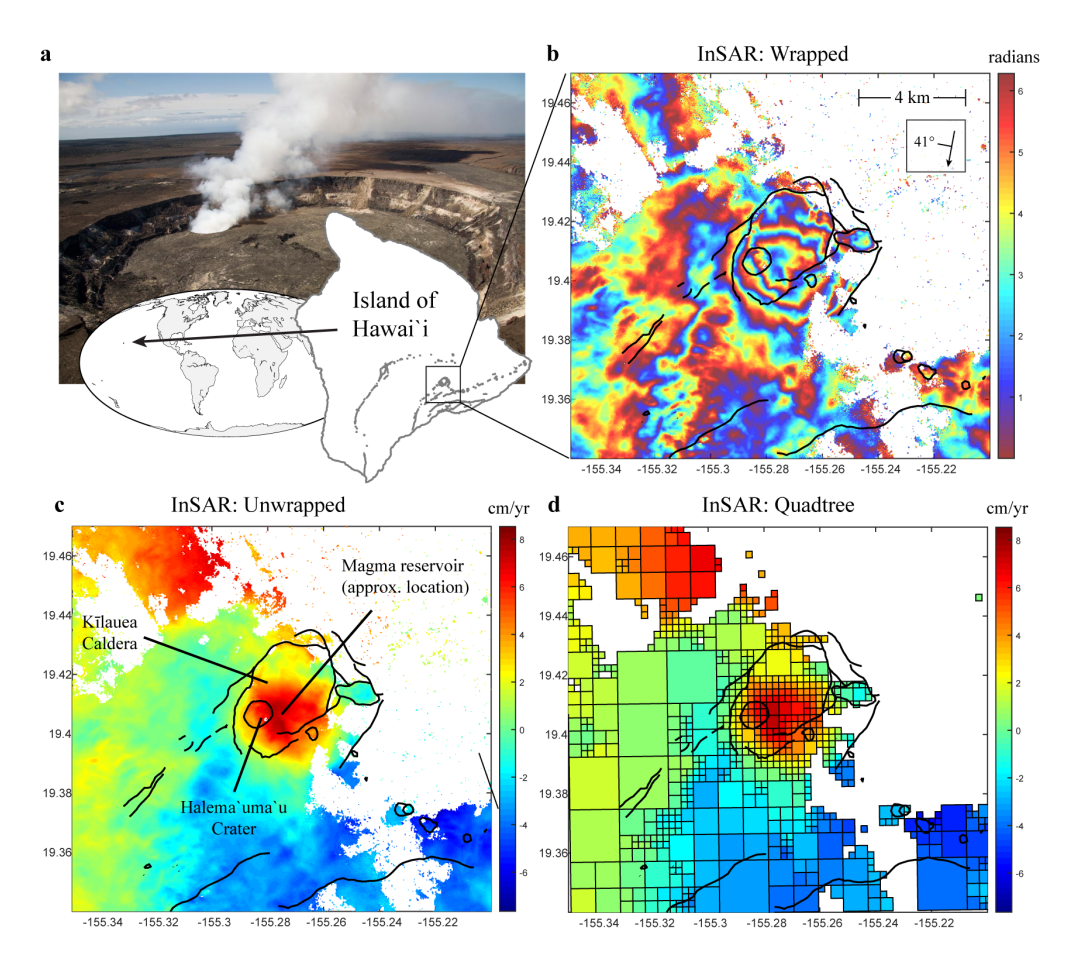


Figure 1: a) Overview maps showing the location of Kīlauea Volcano on the Island of Hawai'i, with background photo of Halema'uma'u Crater at the volcano's summit (USGS photo). (b) Wrapped InSAR interferogram from the COSMO-SkyMed satellite, spanning 20 Oct 2011 to 15 May 2012. The inset box shows the flight path of the satellite (arrow) and the downward look direction of the satellite at 41°. White areas have no data due to radar decorrelation. Number of data points is around  $1.5 \times 10^5$ . (c) Same data as in (b), but unwrapped. (d) Quadtree-processed interferogram. Thick black lines in panels b-d show cliffs and other important topographic features at the volcano; the large elliptical feature is Kīlauea Caldera.

unprecedented rift eruption destroyed more than 700 homes and displaced thousands of residents (Neal et al., 2019). Figure 1 shows ground displacements at Kīlauea from October, 2011 to May, 2012, as the summit of the volcano inflated due to magma storage (Anderson and Poland, 2016). These data were recorded from a satellite orbiting roughly north to south, which recorded LoS deformation along a vector oblique to the Earth's surface – roughly east to west and downwards at an angle of 41 degrees. This image thus resolves a combination of predominantly vertical and east-west ground deformation. In Figure 1d the image was

subsampled by the quadtree algorithm for computational efficiency (Jonsson et al., 2002).

Of the sources of uncertainty in (1), the spatially-correlated atmospheric term  $\phi_a$  is usually the most important; spatial and temporal changes of just 20% in relative humidity can lead to errors of 10 cm in estimated ground deformation (Zebker et al., 1997). Figure 1b shows wrapped InSAR phase at Kīlauea Volcano. A "bullseye" pattern near the center is due to real ground deformation  $\phi_d$ , while most of the remaining fringes are due to  $\phi_a$ .

We highlight a few contributions of this study to address the main challenges and scientific questions for calibration using data from multiple sources. First, the geophysical model considered herein cannot fully explain reality and atmospheric conditions or other sources of bias. Thus, we model both discrepancy and measurement bias functions to improve predictions. Second, we model the discrepancy function by S-GaSP and measure bias by GaSP. Theoretical and numerical results were studied to support this choice. Third, averaging multiple satellite radar images is sometimes used in geophysical studies, but the difference between modeling individual vs. averaged images is not well-studied. Here we derive conditions when these two inferences are equivalent, and provide examples when modeling individual images leads to more precise estimation. Finally, to overcome computational challenges from the large number of pixels in InSAR images, we discuss different downsampling schemes,

The rest of the paper is organized as follows. In Section 2, we discuss differences and connection in modeling aggregated data and individual sources of data. Two approaches of the discrepancy function and measurement bias are compared in Section 3. The parameter estimation via the full Bayesian inference is discussed in Section 4. Simulated and real numerical evidence comparing several models are given in Section 5, and a short conclusion is given in Section 6. Proofs and derivations are provided in the supplementary materials.

# 2 Model calibration by multiple sources of data

In this section, we first introduce a statistical framework for calibrating imperfect mathematical models by multiple data sources. In Section 2.2 we discuss the difference between

modeling full and aggregated data sets. Downsampling schemes are compared in Section 2.3.

#### 2.1 Modeling imperfect measurements from multiple sources

Denote  $y_l^F(\mathbf{x})$  the real-valued field data at the observable input  $\mathbf{x} \in \mathcal{X}$  from the source (e.g. image) l, l = 1, ..., k. The mathematical model is defined as  $f^M(\mathbf{x}, \boldsymbol{\theta})$ , where  $\boldsymbol{\theta}$  denotes unobservable calibration parameters. We both discrepancy and measurement bias below

$$\mathbf{y}_{l}^{F}(\mathbf{x}) = f^{M}(\mathbf{x}, \boldsymbol{\theta}) + \delta(\mathbf{x}) + \delta_{l}(\mathbf{x}) + \mu_{l} + \epsilon_{l}, \tag{2}$$

where  $\mu_l$  is a mean parameter and  $\epsilon_l \sim \mathrm{N}(0, \sigma_{0l}^2)$  is independent Gaussian noise with variance  $\sigma_{0l}^2$ , for each  $\mathbf{x}$  and for l=1,...,k. In model (2),  $\delta(\cdot)$  and  $\delta_l(\cdot)$  denote the model discrepancy and the lth measurement bias function, respectively. For any  $\{\mathbf{x}_1,...,\mathbf{x}_n\}$ , we assume that marginal distributions of  $\boldsymbol{\delta} = (\delta(\mathbf{x}_1),...,\delta(\mathbf{x}_n))^T$  and  $\boldsymbol{\delta}_l = (\delta_l(\mathbf{x}_1),...,\delta_l(\mathbf{x}_n))^T$  follow multivariate normal distributions:  $\boldsymbol{\delta} \sim \mathrm{MN}(\mathbf{0}, \tau^2 \mathbf{R})$  and  $\boldsymbol{\delta}_l \sim \mathrm{MN}(\mathbf{0}, \sigma_l^2 \mathbf{R}_l)$ , where  $\tau^2 \mathbf{R}$  and  $\sigma_l^2 \mathbf{R}_l$  are covariances with variance parameters  $\tau^2$  and  $\sigma_l^2$ , respectively. The (i,j)th terms of  $\mathbf{R}$  and  $\mathbf{R}_l$  are parameterized by kernel functions  $K(\mathbf{x}_i, \mathbf{x}_j)$  and  $K_l(\mathbf{x}_i, \mathbf{x}_j)$ , respectively, for l=1,...,k, and  $1 \leq i,j \leq n$ . We postpone the discussion of kernel functions to Section 3.

In model (2), the physical reality, denoted as  $y^R(\mathbf{x})$  at any coordinate  $\mathbf{x}$ , can be expressed as summation of the mathematical model and discrepancy function, i.e.  $y^R(\mathbf{x}) = f^M(\mathbf{x}, \boldsymbol{\theta}) + \delta(\mathbf{x})$ , which follows the framework in Kennedy and O'Hagan (2001). The innovation in (2) is to explicitly model the measurement bias (spatially correlated pattern) contained in different sources of observations through spatial models.

For our case study, long-wavelength "ramp" artifacts may appear in InSAR interferogram due to errors in satellite orbits. Linear or quadratic ramp parameters may be estimated together with geophysical model parameters if the ramps cannot be corrected independently (for instance using data from GPS sensors) (Simons and Rosen, 2007). Here since the area of geographic area of interest is relatively small, linear and higher-order ramp terms are negli-

gible. Because InSAR measures ground displacements relative to a subjective point assumed to be non-deforming, however, we must account for the uncertainty of the mean value of each image. Thus, we assume an unknown mean parameter  $\mu_l$  of the lth interferogram, for l = 1, ..., k, in model (2). In general, the intercept and trend can be modeled as a mean function in model (2), if they are not captured in the mathematical model.

The closed form marginal distributions and predictive distributions of the discrepancy, measurement bias and the reality of model (2) are given in Section S2 in the supplementary materials. Since the computational complexity of each evaluation of the likelihood increases linearly to k, images are often averaged prior to modeling in geoscience studies to reduce computational cost. We then study the difference these two ways of inferences.

#### 2.2 Model calibration by aggregated data and full data

First consider the data with no measurement bias, that is  $y_l^F(\mathbf{x}) = y^R(\mathbf{x}) + \epsilon_l$ , where  $y^R(\mathbf{x})$  is the fixed, unknown reality. The data can be modeled below

$$y_l^F(\mathbf{x}) = f^M(\mathbf{x}, \boldsymbol{\theta}) + \delta(\mathbf{x}) + \mu + \epsilon_l, \tag{3}$$

where  $\epsilon_l \sim N(0, \sigma_0^2)$  for each  $\mathbf{x}$ , and l = 1, ..., k. Model (3) has been widely used in calibration by repeated experimental responses (Bayarri et al., 2007; Arendt et al., 2012b).

Denote  $\bar{y}^F(\mathbf{x}) = \sum_{l=1}^k y_l^F(\mathbf{x})/k$  the average value of the field data at the input  $\mathbf{x}$ . When (3) is assumed, the model of the aggregated data follows

$$\bar{y}^F(\mathbf{x}) = f^M(\mathbf{x}, \boldsymbol{\theta}) + \delta(\mathbf{x}) + \mu + \bar{\epsilon},$$
 (4)

where  $\bar{\epsilon} \sim N(0, \sigma_0^2/k)$  independently for each  $\mathbf{x}$ . Denote  $\mathbf{y}_l^F = (y_l^F(\mathbf{x}_1), ..., y_l^F(\mathbf{x}_n))^T$  the observations in source l, and  $\bar{\mathbf{y}}^F = (\sum_{l=1}^k y_l^F(\mathbf{x}_1)/k, ..., \sum_{l=1}^k y_l^F(\mathbf{x}_n)/k)^T$  the aggregated data. Although  $\bar{\mathbf{y}}^F$  is often used geophysical studies, the relation between modeling the aggregated data (e.g. stacked image) in (4) versus modeling full data in (3) is not generally known.

**Lemma 1.** Integrating out  $\delta \sim MN(\mathbf{0}, \tau^2 \mathbf{R})$ , the natural logarithm of the marginal likelihood in model (3) follows

$$\ell(\boldsymbol{\theta}, \mu, \sigma_0^2, \tau, \mathbf{R}) = c_{\sigma_0^2} + \bar{\ell}(\boldsymbol{\theta}, \mu, \sigma_0^2), \tag{5}$$

where  $c_{\sigma_0^2} = -\frac{n(k-1)}{2}\log(2\pi\sigma_0^2) - \frac{n}{2}\log(k) - \frac{\sum_{l=1}^k\sum_{i=1}^n(y_l^F(\mathbf{x}_i) - \bar{y}^F(\mathbf{x}_i))^2}{2\sigma_0^2}$  and  $\bar{\ell}(\boldsymbol{\theta}, \mu, \sigma_0^2)$  is the natural logarithm of the marginal likelihood model from (4), after integrating out  $\boldsymbol{\delta}$ :

$$\bar{\ell}(\boldsymbol{\theta}, \mu, \sigma_0^2, \tau, \mathbf{R}) = -\frac{n}{2}\log(2\pi) - \frac{1}{2}\log\left|\tilde{\mathbf{\Sigma}}\right| - \frac{(\bar{\mathbf{y}}^F - \mu\mathbf{1} - \mathbf{f}_{\boldsymbol{\theta}}^M)^T\tilde{\mathbf{\Sigma}}^{-1}(\bar{\mathbf{y}}^F - \mu\mathbf{1} - \mathbf{f}_{\boldsymbol{\theta}}^M)}{2},$$

where 
$$\tilde{\Sigma} = \tau^2 \mathbf{R} + \frac{\sigma_0^2}{k} \mathbf{I}_n$$
.

When the covariance  $\tilde{\Sigma}$  is known, Equation (5) implies some frequently used estimators, such as the maximum likelihood estimator (MLE) of  $\boldsymbol{\theta}$  and  $\mu$  by aggregated data, are exactly the same as modeling the full data in (3). This result also holds when there is no discrepancy in the model (or equivalently  $\tau^2 = 0$ ). This validates the use of stacked image for estimating the calibration parameters and mean parameter, when the covariance of residuals is known, as the aggregated data  $\bar{\mathbf{y}}^F$  is the sufficient statistics of calibration parameters.

When covariance  $\tilde{\Sigma}$  is unknown, the sufficient statistics of model (3) is  $(\bar{\mathbf{y}}^F, s^2)$ , where  $s^2 = \sum_{l=1}^k \sum_{i=1}^n (y_l^F(\mathbf{x}_i) - \bar{y}^F(\mathbf{x}_i))^2$ . This result was previously discussed in Bayarri et al. (2007). However, the efficiency of estimators based on full and aggregated data was not compared. For instance, the usual unbiased estimator of  $\sigma_0^2$  based on the full data is the sample variance  $s^2/(n(k-1))$ , which has the variance  $2\sigma_0^4/(n(k-1))$  in estimating  $\sigma_0^2$ , if the reality  $y^R(\cdot)$  is an unknown, fixed function. For aggregated data modeled in (4), assuming that the reality  $y^R(\cdot)$  is known, the unbiased, oracle estimator of  $\sigma_0^2$  is  $k \sum_{i=1}^n (\bar{y}^F(\mathbf{x}_i) - y^R(\mathbf{x}_i))^2/n$ , which has variance  $2\sigma_0^4/n$ , much larger than the sample variance based on full data when k is large. Since reality  $y^R(\cdot)$  is unknown, the variance of the unbiased estimator of  $\sigma_0^2$  typically becomes even larger. Thus, modeling aggregated data in (4) is less efficient in estimating covariance parameters, such as  $\sigma_0^2$ , than modeling the full data in (3).

When  $k \to \infty$ , the limiting distribution of  $\bar{\mathbf{y}}^F$  in (4) follows

$$(\bar{\mathbf{y}}^F \mid \mu, \boldsymbol{\theta}, \tau^2, \mathbf{R}) \sim \text{MN} (\mathbf{f}_{\boldsymbol{\theta}}^M + \mu \mathbf{1}_n, \tau^2 \mathbf{R}).$$
 (6)

Note that under some sensible assumptions, e.g. assuming  $\lim_{k\to\infty} \frac{1}{k} \sum_{l=1}^k \mu_l = \mu < \infty$ ,  $\sigma_0^2 < \infty$  and  $\lim_{k\to\infty} \frac{1}{k} \sum_{l=1}^k \tilde{\Sigma}_l < \infty$ , where  $\tilde{\Sigma}_l = \sigma_l^2 \mathbf{R}_l + \sigma_{0l}^2 \mathbf{I}_n$ , the limiting distribution of the aggregated data  $\bar{\mathbf{y}}^F$  in model (2) with measurement bias and different mean parameters also follows equation (6). Thus the inference based on the aggregate data and full data becomes similar when the number of sources of data goes to infinity.

#### 2.3 Downsampling satellite interferograms

A single InSAR image is often composed of hundreds of thousands of pixels. Even for very simple geophysical models, the expense of computing deformation at all these points can be prohibitive, and subsampling techniques are typically employed. One approach is to uniformly sample a subset of pixels for calibration and prediction (Pritchard et al., 2002). Posterior distributions of calibration parameters are often stable with responses at only a few hundred pixels (Gu and Wang, 2018).

Another method for downsampling is the quadtree algorithm, where one computes the average (or median) of boxes of pixels, whose sizes are based on gradients in the image (Simons et al., 2002), the resolution of the forward model (Lohman and Simons, 2005), or both (Wang et al., 2014). These algorithms have become widely used for InSAR processing for data inversion (e.g. Montgomery-Brown et al., 2015; Anderson et al., 2019).

Because the boxes in a quadtree-processed image, such as in Figure 1d, are computed from different numbers of pixels, in a calibration problem it is therefore important to take into account the size of the quadtree boxes in modeling (Simons et al., 2002; Lohman and Simons, 2005). However, this seems to have been overlooked in many previous studies using quadtree-processed InSAR data for model calibration and prediction.

Suppose we have  $J_l$  boxes of the lth quadtree-processed image, each box having  $n_{j,l}$  pixels, for  $j=1,...,J_l$  and l=1,...,k. Denote the lth quadtree-processed image by  $\mathbf{y}_l^{F,Q} := \{y_l^{F,Q}(\mathbf{x}_{S_{1,l}}),...,y_l^{F,Q}(\mathbf{x}_{S_{J_l,l}})\}$ , where  $S_{j,l}$  is the set of indices of the pixels contained in the jth box in the image. Let  $\mu_l^Q$ ,  $f^{M,Q}(\mathbf{x}_{S_{j,l}},\boldsymbol{\theta})$ ,  $\delta^Q(\mathbf{x}_{S_{j,l}})$  and  $\delta_l^Q(\mathbf{x}_{S_{j,l}})$  denote the corresponding mean parameter, outputs of the mathematical model, discrepancy function, measurement bias function evaluated at the centroid of jth box at the lth quadtree-processed image, for  $j=1,...,J_l$ , and l=1,...,k. Consider the model of the quadtree-processed image l:

$$y_l^{F,Q}(\mathbf{x}_{S_{j,l}}) \sim \mathcal{N}(f^M(\mathbf{x}_{S_{j,l}}, \boldsymbol{\theta}) + \delta(\mathbf{x}_{S_{j,l}}) + \mu_l + \delta_l(\mathbf{x}_{S_{j,l}}), \frac{\sigma_0^2}{\omega_{j,l}}), \tag{7}$$

with weight  $\omega_{j,l}$  for the jth image and lth source of data,  $j = 1, ..., J_l$  and l = 1, ..., k. Model (7) of the quadtree-processed image is the same as model (2) of the original images if

$$\sum_{i \in S_{j,l}} (y_l^F(\mathbf{x}_i) - f^M(\mathbf{x}_i, \boldsymbol{\theta}) - \delta(\mathbf{x}_i) - \delta_l(\mathbf{x}_i) - \mu_l)^2$$

$$= \omega_{j,l} (y^{F,Q}(\mathbf{x}_{S_{j,l}}) - f^{M,Q}(\mathbf{x}_{S_{j,l}}, \boldsymbol{\theta}) - \delta^Q(\mathbf{x}_{S_{j,l}}) - \delta_l^Q(\mathbf{x}_{S_{j,l}}) - \mu_l^Q)^2.$$
(8)

for  $j=1,...,J_l$  and l=1,...,k. In general, equation (8) is hard to enforce in practice, as one does not know the discrepancy and measurement bias functions apriori. Some previous weighting schemes utilize the estimated covariance structure of the InSAR data (Lohman and Simons, 2005). In this work we follow (Simons et al., 2002; Anderson and Poland, 2016) to let the weight of each quadtree box proportional to the number of the pixels in the box, i.e.  $\omega_{j,l} \propto n_{j,l}$  for  $j=1,...,J_l$ . Both downsampling schemes will be compared in Section 5.2.

## 3 Models of model discrepancy and measurement bias

The discrepancy function is often modeled as a GaSP (Kennedy and O'Hagan, 2001):

$$\delta(\cdot) \sim \text{GaSP}(0, \tau^2 K(\cdot, \cdot)),$$
 (9)

where  $\tau^2K(\cdot,\cdot)$  is a covariance function with variance  $\tau^2$ . The identifiability issue, however, has been widely observed in modeling spatially correlated data, where the spatial random effect was confounded with a linear fixed effect, i.e.  $f^M(\mathbf{x}, \boldsymbol{\theta})$  being a linear model of  $\boldsymbol{\theta}$ , (Reich et al., 2006; Hodges and Reich, 2010; Zhang, 2004). The identifiability of the calibration parameters was also recently realized when the discrepancy function is modeled by a GaSP (Arendt et al., 2012a; Tuo and Wu, 2015, 2016; Plumlee, 2017; Wong et al., 2017), where the calibrated physical models can be far away from reality in terms of  $L_2$  distance.

In previous studies (Bayarri et al., 2007; Arendt et al., 2012b), it was found that repeated observations help identifiability, as the estimation of variance of the data improves, which coincide our discussion in Section 2.1. However, it is rarely realized that even if we have infinite sources and each source contains infinite data, the usual estimator of the calibration parameters, such as the MLE, is not even consistent. Here we provide a closed-form example.

**Example 1.** Assume field data of the source l at input  $x_i$  follows

$$y_l^F(x_i) = f^M(x_i, \theta) + \delta(x_i) + \epsilon_l,$$

where  $f^M(x_i, \theta) = \theta$ ,  $\delta(\cdot) \sim GaSP(0, \tau^2K(\cdot, \cdot))$ , with  $K(x_i, x_j) = \exp(-|x_i - x_j|/\gamma)$ , and  $\epsilon_l \sim N(0, \sigma_0^2)$  is an independent Gaussian noise for each  $x_i$ , i = 1, ..., n, and for l = 1, ..., k. Assume the observations  $y_l^F(x_i)$  are equally spaced from [0, 1], i.e.  $x_i = (i - 1)/(n - 1)$ , for i = 1, ..., n and l = 1, ..., k. Further assume  $\gamma$ ,  $\tau^2$  and  $\sigma_0^2$  are known and finite.

The following results show that MLE is an inconsistent estimator of  $\theta$  in this scenario.

**Lemma 2.** Assume  $\tau^2 > 0$  and  $\gamma > 0$  are both finite. When  $n \to \infty$  and  $k \to \infty$ , after integrating out  $\delta$ , the MLE of  $\theta$  in Example 1 has the limiting distribution:

$$\hat{\theta}_{MLE} \sim N(\theta, \frac{2\tau^2 \gamma}{2\gamma + 1}).$$
 (10)

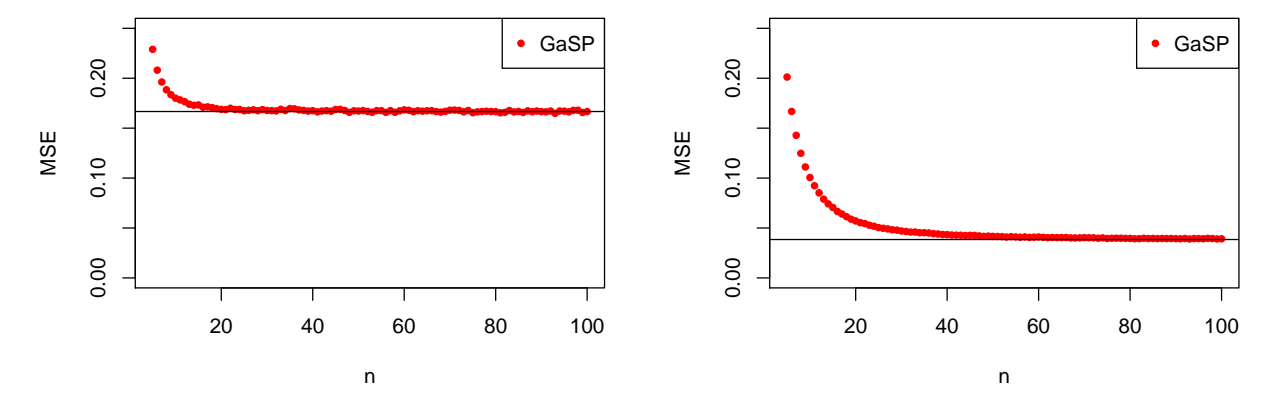


Figure 2: Mean squared error (MSE) of the MLE of  $\theta$  in Example 1 for different numbers of observations when k is large. The limiting variance of the MLE for GaSP data in Lemma 2 is graphed as the black horizontal lines.  $10^5$  simulations are implemented to calculate each value. The range parameter is assumed to be  $\gamma = 0.1$  and  $\gamma = 0.02$  in the left and right panels, respectively, both assuming  $\tau_0^2 = 1$ .

The result in Lemma 2 is surprising as both k and n go to infinity, yet reasonable, because the discrepancy function is shared across all experiments. Thus, even if the estimation of the summation of the model output and discrepancy (i.e. the reality) is consistent, the estimation of the calibration parameters or discrepancy function is often inconsistent.

The MSE between the MLE of  $\theta$  and truth in Example 1 is graphed as the red triangles at different number of observations in Figure 2 when  $k \to \infty$ . In the left panel, when  $\gamma = 0.1$ , the MSE quickly converges when the sample size increases. In the right panel, the MSE converges to a smaller value when  $\gamma = 0.02$ , because the correlation is smaller. Both MSEs converge to the limiting value,  $\frac{2\tau^2\gamma}{2\gamma+1}$  (black horizontal line), found in Lemma 2.

Though the closed-form expression of the limiting distribution of the MLE of the parameter in Lemma 2 relies on the exponential kernel function, the MLE is inconsistent for the mean parameter of the GaSP model with many other kernel functions, such as the Matérn kernel. We refer the reader to Chapter 4.2 in Stein (2012) for the detailed discussion in this topic. Example 1 points out that even infinite number of repeated samples cannot solve the identifiability problem between calibration parameters and discrepancy function.

#### 3.1 Discretized scaled Gaussian stochastic process of discrepancy

When the discrepancy function is modeled by a GaSP, the  $L_2$  loss between the mathematical model and reality is  $L_2(\boldsymbol{\theta}) = \int_{\mathbf{x} \in \mathcal{X}} \delta^2(\mathbf{x}) d\mathbf{x}$ , a random variable whose measure is induced by the covariance function of GaSP. Using some routinely used covariance functions, the distribution of  $L_2(\boldsymbol{\theta})$  can have large probability mass at large  $L_2$  loss when the correlation in the data is large. Because of this reason, we propose to model the discrepancy function by the discretized S-GaSP introduced in Gu and Wang (2018):

$$\delta_z(\mathbf{x}) = \left\{ \delta(\mathbf{x}) \mid \frac{1}{n} \sum_{i=1}^n \delta^2(\mathbf{x}_i) = Z \right\},$$

$$\delta \sim \text{GaSP}(0, \tau^2 K(\cdot, \cdot)), \ Z \sim p_{\delta_z}(\cdot),$$
(11)

where  $p_{\delta_z}(\cdot)$  is the density of the random squared error between the reality and mathematical model. Given Z = z, S-GaSP is a GaSP constrained at the space  $\sum_{i=1}^{n} \frac{\delta^2(\mathbf{x}_i)}{n} = z$ . The idea is to assign more probability mass on the small squared error by  $p_{\delta_z}(\cdot)$  defined later.

Denote  $p_{\delta}(Z = z \mid \boldsymbol{\gamma}, \tau^2)$  the density of Z = z induced by the GaSP model in (9), where  $\tau^2$  and  $\boldsymbol{\gamma}$  are the variance parameter and range parameters in the covariance function, respectively. We let  $p_{\delta_z}(\cdot)$  proportional to  $p_{\delta}(\cdot)$ , but scaled by a non-increasing function:

$$p_{\delta_z}(Z=z|\boldsymbol{\gamma},\tau^2,\lambda_z) = \frac{f_Z(Z=z\mid \tau^2,\lambda_z) p_{\delta}(Z=z\mid \boldsymbol{\gamma},\tau^2)}{\int_0^\infty f_Z(Z=t\mid \tau^2,\lambda_z) p_{\delta}(Z=t\mid \boldsymbol{\gamma},\tau^2) dt},$$
(12)

where  $f_Z(Z=z\mid \tau^2, \lambda_z)$  is a non-increasing function depending on  $\tau^2$  and scaling parameter  $\lambda_z$ , at all  $z\geq 0$ . We let  $f_Z(\cdot)$  be an exponential distribution for computational reasons:

$$f_Z(Z = z \mid \tau^2, \lambda_z) = \frac{\lambda_z}{2\tau^2 \text{Vol}(\mathcal{X})} \exp\left(-\frac{\lambda_z z}{2\tau^2 \text{Vol}(\mathcal{X})}\right),$$
 (13)

where  $\lambda_z$  is a positive scaling parameter and  $\operatorname{Vol}(\mathcal{X})$  is the volume of the input domain  $\mathcal{X}$ .

The GaSP with any covariance function is a special case of S-GaSP when  $f_Z(\cdot)$  is a constant function, or equivalently  $\lambda_z = 0$ . On the other hand, starting from a GaSP model

with any reasonable covariance function  $\tau^2 K(\cdot, \cdot)$ , after marginalizing out Z, it was shown in Gu and Wang (2018) that the marginal distribution of  $\boldsymbol{\delta}_z := (\delta_z(\mathbf{x}_1), ..., \delta_z(\mathbf{x}_n))^T$  follws a multivariate normal distribution with a transformed covariance matrix:

$$\delta_z \mid \Theta \sim \text{MN}(\mathbf{0}, \tau^2 \mathbf{R}_z),$$
 (14)

where  $\mathbf{R}_z = \left(\mathbf{R}^{-1} + \frac{\lambda_z}{n} \mathbf{I}_n\right)^{-1}$  and the (i, j)th term of  $\mathbf{R}$  is  $K(\mathbf{x}_i, \mathbf{x}_j)$ . Note that  $\mathbf{R}_z$  is different from a covariance matrix with a nugget parameter.

A larger  $\lambda_z$  assigns more prior probability on the smaller sum of squares of the discrepancy function. Under some regularity conditions, a suitable choice of  $\lambda_z$  guarantees the predictive distribution in the S-GaSP model converges to the reality as fast as in the GaSP model, and the estimation of the calibration parameters in the S-GaSP model minimizes the  $L_2$  loss between the reality and mathematical model, when the sample size goes to infinity. In all numerical examples, we let  $\lambda_z = C\sqrt{n}$ , with C = 100, which guarantees two convergence properties under common regularity conditions (Gu et al., 2018b).

The S-GaSP was inspired by a series of pioneering works aiming to minimize the  $L_2$  distance between reality and mathematical models (Tuo and Wu, 2015, 2016; Plumlee, 2017; Wong et al., 2017). the comparison between S-GaSP and these approaches are studied in e.g. (Gu et al., 2018b). The focus of this work is on modeling measurement bias and discrepancy simultaneously, which was not discussed in previous studies.

## 3.2 Gaussian stochastic process of measurement bias

Gaussian random fields were widely used to model spatially correlated data (Banerjee et al., 2014), and hence we model the measurement bias  $\delta_l(\cdot)$  via GaSPs below:

$$\delta_l(\cdot) \sim \text{GaSP}(0, \sigma_l^2 K_l(\cdot, \cdot)),$$
 (15)

where  $K_l(\cdot, \cdot)$  is the kernel function for l = 1, ..., k, meaning that for any  $\{\mathbf{x}_1, ..., \mathbf{x}_n\}$ , the marginal distribution of  $\boldsymbol{\delta}_l$  follows a multivariate normal distribution with covariance  $\sigma_l^2 \mathbf{R}_l$ , for l = 1, ..., k, with the (i, j)th term of  $\mathbf{R}_l$  being  $K_l(\mathbf{x}_i, \mathbf{x}_j)$ . For any inputs  $\mathbf{x}_a := (x_{a1}, ..., x_{ap})$  and  $\mathbf{x}_b := (x_{b1}, ..., x_{bp})$ , we assume a product covariance (Bayarri et al., 2007)

$$K_l(\mathbf{x}_a, \mathbf{x}_b) = \prod_{t=1}^p K_{l,t}(x_{at}, x_{bt}), \tag{16}$$

where each  $K_{l,t}(\cdot,\cdot)$  is a one-dimensional kernel function for correlation between the  $t^{th}$  coordinate of any two inputs for the source l, l = 1, ..., k. Denote  $d_t = |x_{at} - x_{bt}|$ . One popular choice is the Matérn correlation, which has a closed form expression with the roughness parameter  $\alpha_t = (2k+1)/2$  for  $k \in \mathbb{N}$ . E.g., the Matérn correlation function with  $\alpha_t = 5/2$  is (Handcock and Stein, 1993; Guttorp and Gneiting, 2006):

$$K_{l,t}(d_t) = \left(1 + \frac{\sqrt{5}d_t}{\gamma_t} + \frac{5d_t^2}{3\gamma_l^2}\right) \exp\left(-\frac{\sqrt{5}d_t}{\gamma_t}\right). \tag{17}$$

A desirable feature of the Matérn correlation is that the sample path of the process is  $\lfloor \alpha_l \rfloor$  differentiable. In relation to the present scientific goal, we also note that previous works have argued that Matérn correlation functions are suitable for modeling atmospheric noise in InSAR data (Knospe and Jonsson, 2010). However, we do not limit ourselves to any specific correlation function and the methods discussed in this work apply to all such functions.

# 4 Parameter estimation using multiple sources of data

The S-GaSP model of the lth interferogram, l = 1, ..., k, is defined below

$$\mathbf{y}_{l}^{F}(\mathbf{x}) = f^{M}(\mathbf{x}, \boldsymbol{\theta}) + \delta_{z}(\mathbf{x}) + \delta_{l}(\mathbf{x}) + \mu_{l} + \epsilon_{l}. \tag{18}$$

The only different between the S-GaSP calibration model in (18) and the GaSP calibration

Table 1: Input variables, calibration parameters of the geophysical model and other model parameters in calibration.

parameters in campration.	
Input variables $(\mathbf{x})$	Description
$x_1$	East-west spatial coordinate
$x_2$	North-south spatial coordinate
Calibration parameters $(\boldsymbol{\theta})$	Description
$\theta_1 \in [-2000, 3000]$	East-west spatial coordinate of chamber centroid $(m)$
$\theta_2 \in [-2000, 5000]$	North-south spatial coordinate of chamber centroid $(m)$
$\theta_3 \in [500, 6000]$	Depth of the chamber $(m)$
$\theta_4 \in [0, 0.15]$	Volume change rate of the reservoir $(m^3/s)$
$\theta_5 \in [0.25, 0.33]$	Poisson's ratio (host rock property)
Model parameters	Description
$\boldsymbol{\mu} = (\mu_1,,\mu_k)$	mean parameters
$\boldsymbol{\beta}_{1:k} = (\beta_{1,1},, \beta_{1,p},, \beta_{k,1},, \beta_{k,p})$	inverse range parameters of the measurement bias
$oldsymbol{\eta} = (\eta_1,, \eta_k)$	nugget parameters of the measurement bias
$oldsymbol{\sigma}^2 = (\sigma_1^2,,\sigma_k^2)$	scale parameters of the measurement bias
$oldsymbol{eta}=(eta_1,,eta_p)$	range parameters of the model discrepancy
$ au^2$	scale parameter of the model discrepancy

model in (2) is on the discrepancy function, assumed to follow a discretized S-GaSP in (11) and a GaSP in (9), respectively. Note that the marginal distribution in the S-GaSP calibration is a multivariate normal distribution with the covariance matrix  $\tau^2 \mathbf{R}_z$ . Thus, likelihood and predictive distributions derived for the GaSP calibration in Section S2 of supplementary materials can be used in the S-GaSP calibration, only replacing  $\mathbf{R}$  by  $\mathbf{R}_z$ .

The parameters in (2) and (18) both contain the calibration parameters, mean parameters, variance parameters of noises, range and scale parameters of the model discrepancy and measurement bias functions. For computational purposes, we transform the variance parameter  $\sigma_{0l}^2$  to define the nugget parameter  $\eta_l := \sigma_{0l}^2/\sigma_l^2$ , for l=1,...,k. By definition,  $\sigma_{0l}^2$  becomes the overall scale parameter of the matrix  $\tilde{\Sigma}_l$  in Lemma S1 which has a conjugate prior that simplifies the computation. We also transform to define the inverse range parameter  $\beta_t = 1/\gamma_t$ , for t=1,...,p, and  $\beta_{l,t} = 1/\gamma_{l,t}$ , for l=1,...,k and t=1,...,p.

The input variables, calibration parameters and other model parameters are listed in Table 1 for calibrating the geophyiscal model for Kīlauea Volcano using multiple interferograms.

We assume the prior below:

$$\pi(\boldsymbol{\theta}, \boldsymbol{\mu}, \boldsymbol{\beta}_{1:k}, \boldsymbol{\eta}, \boldsymbol{\sigma}^2, \boldsymbol{\beta}, \tau^2) \propto \frac{\pi(\boldsymbol{\theta})\pi(\boldsymbol{\beta})}{\tau^2} \prod_{l=1}^k \left\{ \frac{\pi(\boldsymbol{\beta}_l, \eta_l)}{\sigma_l^2} \right\}, \tag{19}$$

The prior of the calibration parameters  $\boldsymbol{\theta}$  often depends on experts' knowledge, as the calibration parameters have scientific meanings. For calibrating the geophysical model of Kīlauea Volcano, we assume  $\pi(\boldsymbol{\theta})$  a uniform distribution on the domain of the calibration parameters, listed in Table 1. The mean and scale parameters are assigned a usual location-scale prior in (19), i.e.  $\pi(\tau^2) \propto 1/\tau^2$  and  $\pi(\mu_l, \sigma_l^2) \propto 1/\sigma_l^2$ , for l = 1, ..., k. Furthermore, we assume the jointly robust prior for the range and nugget parameters in both the measurement bias functions and discrepancy function Gu (2018).

The geophysical model used in this study is computationally inexpensive, but that is often not the case (e.g., Anderson and Segall, 2011). In such cases, a statistical emulator may be used to approximate the geophysical model based on a limited set of model runs on some prespecified inputs. We implemented the full Bayesian analysis of calibration and prediction using both the GaSP and discretized S-GaSP discrepancy models in an R package, called RobustCalibration, available on CRAN. The robust GaSP emulator Gu (2018) is implemented in the RobustCalibration package for use when the mathematical model is computationally expensive. Although we focus on using satellite interferograms for calibration, the methodology and the R package provide a general statistical framework for combining multiple sources of data for calibration and prediction.

## 5 Numerical studies

# 5.1 Simulated examples

We first discuss an example without measurement bias to compare the identifiability issue between GaSP and S-GaSP models of discrepancy function.

Table 2: Predictive mean squared errors and the MLE of the parameters in GaSP and S-GaSP calibration models in Example 2.

	$\mathrm{MSE}_{f^M}$	$\mathrm{MSE}_{f^M+\delta}$	$\hat{m{ heta}}$	$\hat{ au}^2$	$\hat{m{\gamma}}$	$\hat{\sigma}_0^2$
GaSP	91.5	$6.12 \times 10^{-3}$	(13.2, 1.90)	$1.32 \times 10^{2}$	(1.44, 1.8)	$1.76 \times 10^{-3}$
S-GaSP	1.58	$5.47 \times 10^{-3}$	(3.76, 2.01)	$3.54 \times 10^2$	(1.72, 2.13)	$1.74 \times 10^{-3}$

**Example 2.** Assume  $y^F(\mathbf{x}) = y^R(\mathbf{x}) + \epsilon$  where  $\mathbf{x} = (x_1, x_2) \in [0, 1]^2$ ,  $\epsilon \sim N(0, 0.05^2)$  is an independent Gaussian noise for each  $\mathbf{x}$  and reality is assumed to be (Lim et al., 2002):

$$y^{R}(\mathbf{x}) = \frac{1}{6} \left\{ (30 + 5x_1 \sin(5x_1))(4 + \exp(-5x_2)) - 100 \right\}.$$

Let  $f^M(\mathbf{x}, \boldsymbol{\theta}) = \theta_1 + \theta_2 \sin(5x_1)$ , where  $\boldsymbol{\theta} = (\theta_1, \theta_2)$  are unknown calibration parameters. Field data  $y^F(\mathbf{x}_i)$  at  $\mathbf{x}_i$ , i = 1, ..., 30, is drawn from the maximin Latin hypercube design (Santner et al., 2003). The goal is to estimate  $\boldsymbol{\theta}$  and predict the reality at all  $\mathbf{x} \in [0, 1]^2$ .

For Example 2, the true values of the calibration parameters are not well-defined because the discrepancy function is a deterministic function. We thus compare the GaSP and S-GaSP calibrations by the predictive performance based on two criteria of predictions on  $y^R(\mathbf{x}_i^*)$  at the held-out  $\mathbf{x}_i^*$ , uniformly sampled from  $[0,1]^2$  for i=1,...,1000 below:

$$MSE_{f^{M}} = \frac{1}{n^{*}} \sum_{i=1}^{n^{*}} (f^{M}(\mathbf{x}_{i}^{*}, \hat{\boldsymbol{\theta}}) - y^{R}(\mathbf{x}_{i}^{*}))^{2} \quad \text{and} \quad MSE_{f^{M} + \delta} = \frac{1}{n^{*}} \sum_{i=1}^{n^{*}} (\hat{y}^{R}(\mathbf{x}_{i}^{*}) - y^{R}(\mathbf{x}_{i}^{*}))^{2}$$

where  $\hat{\theta}$  are estimated calibration parameters and  $\hat{y}^R(\mathbf{x}_i^*)$  is the prediction of the reality combining mathematical model and discrepancy function. Only the calibrated mathematical model is used to predict the reality in calculating  $MSE_{f^M}$ , whereas both the calibrated mathematical model and discrepancy function for predictions can used to calculate  $MSE_{f^M+\delta}$ .

The predictive error of Example 2 using two models is given in Table 2, where parameters are estimated by the MLE via the low-storage quasi-Newton optimization method (Nocedal, 1980) with 10 different initializations. The  $MSE_{f^M+\delta}$  is similar using both GaSP and S-GaSP calibration, while  $MSE_{f^M}$  by S-GaSP is much smaller than the one by GaSP.

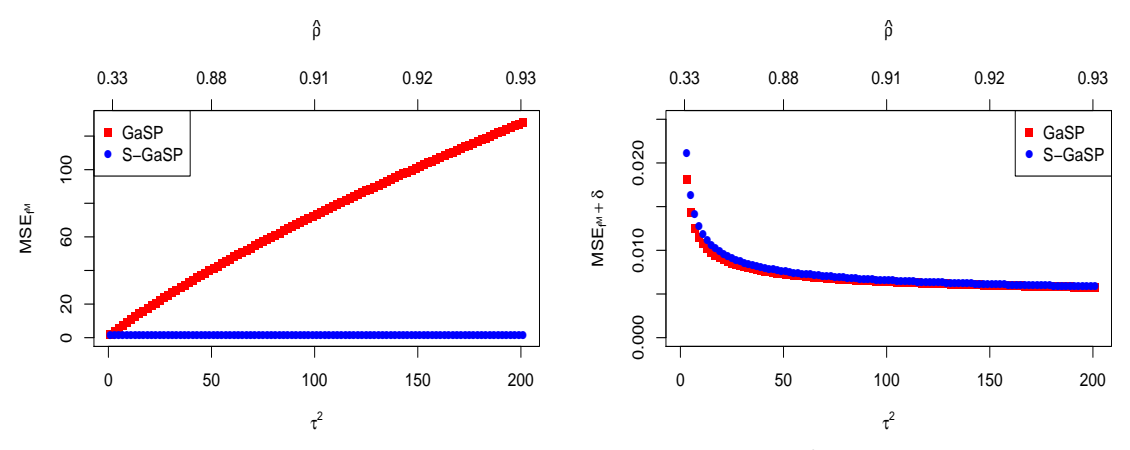


Figure 3: Predictive mean squared errors of Example 2 when  $\tau^2$  is fixed (lower x coordinate) in the GaSP and S-GaSP calibrations. The upper x coordinate is the estimated median value of the correlation matrix  $\mathbf{R}$  for each  $\tau^2$  in the GaSP calibration model.

Denote  $\rho$  the median value in the correlation matrix  $\mathbf{R}$  and let  $\hat{\rho}$  be the estimated value in the GaSP calibration model. After plugging in  $\hat{\gamma}$  in Table 2, we found  $\hat{\rho} \approx 0.92$ , indicating relatively large estimated correlation. To further explore the cause of the large  $\mathrm{MSE}_{f^M}$  in the GaSP calibration, we fix the scale parameter  $\tau^2$  at different values and estimate the rest of the parameters by the MLE in the GaSP calibration. We use the same estimated parameters in the covariance matrix in the S-GaSP calibration and MLE for the calibration parameters. The  $\mathrm{MSE}_{f^M}$  and  $\mathrm{MSE}_{f^M+\delta}$  due to the change of  $\tau^2$  are shown in Figure 3. When  $\tau^2$  is fixed at a small value, the median estimated correlation in the GaSP calibration, shown in the upper x coordinate in Figure 3, is small. When the correlation is small, the  $\mathrm{MSE}_{f^M}$  is small (left panel), whereas the  $\mathrm{MSE}_{f^M+\delta}$  is comparatively large (right panel). When  $\tau^2$  is fixed at a large value, the  $\mathrm{MSE}_{f^M+\delta}$  becomes small by both models, whereas the  $\mathrm{MSE}_{f^M}$  becomes incredibly large in the GaSP calibration due to the large estimated correlation. The  $\mathrm{MSE}_{f^M}$  is always small in the S-GaSP model, shown in Figure 3.

Example 2 shows that the calibrated mathematical model can be far from the reality in the GaSP model, when the estimated correlation is large. When the correlation is small, the predictive distribution of the mathematical model and discrepancy function may sometimes be less precise to predict the reality in this scenario. In comparison, the calibrated mathematical model by the S-GaSP calibration is still close to the reality when the correlation is large. Thus the small  $MSE_{f^M}$  and  $MSE_{f^M+\delta}$  may not be simultaneously obtained in the GaSP model, but they can be achieved at the same time in the S-GaSP calibration.

Next we compare calibration using full and aggregated data with measurement bias.

**Example 3.** Assume data are sampled from model (2), where  $f^M(x,\theta) = \sin(\theta x)$ , with  $\theta = \pi/2$ . The model discrepancy and measurement bias are assumed to follow  $\delta \sim \text{MN}(\mathbf{0}, \tau^2 \mathbf{R})$  and  $\delta_l \sim \text{MN}(\mathbf{0}, \sigma_l^2 \mathbf{R}_l)$ , where  $\tau = 0.2$ ,  $\sigma_l = 0.4 + 0.4(l-1)/(k-1)$ ,  $\mathbf{R}$  and  $\mathbf{R}_l$  both parameterized by the Matérn kernel in (17) with  $\gamma = 0.1$  and  $\gamma_l = 0.02$ , respectively. The standard deviation of the noise is  $\sigma_{0l} = 0.05$  and the observations are equally spaced at  $x_i \in [0,1]$  for i=1,...,n and l=1,...,k. We let n=100 and implement N=200 experiments at three configurations with k=5, k=10 and k=15.

In Example 3, the GaSP calibration model is the true sampling model. Here we compare three models. The first and second approaches are the GaSP calibration and S-GaSP calibration based on the full data, where the discrepancy function is modeled by GaSP in (9) and the discretized S-GaSP model in (11), respectively. The measurement bias functions are assumed to follow GaSPs in both models. Also included is the GaSP calibration by the aggregated data, i.e. the averages of all sources of data. For each approach, we draw 20,000 posterior samples of the parameters, with the first 4,000 posterior samples used as the burn-in samples. To reduce storage space, we thin posterior samples by 10 times.

The mean square error (MSE) of measurement bias, discrepancy functions, reality and the squared error (SE) of the calibration parameter of each experiment by different approaches for Example 3 are shown in Figure 4. First, even though the data is sampled from the GaSP calibration model, the MSEs of the S-GaSP calibration and GaSP calibration are similar in estimation. Second, both methods based on the full data are better than the GaSP calibration based on the aggregated data, as averaging different sources of data causes loss of information due to the presence of the measurement bias and the unknown variance of the noise. Estimation of the calibration parameter by three methods is similar. When the number of sources of data increases, all methods become more accurate in estimation. Decrease of

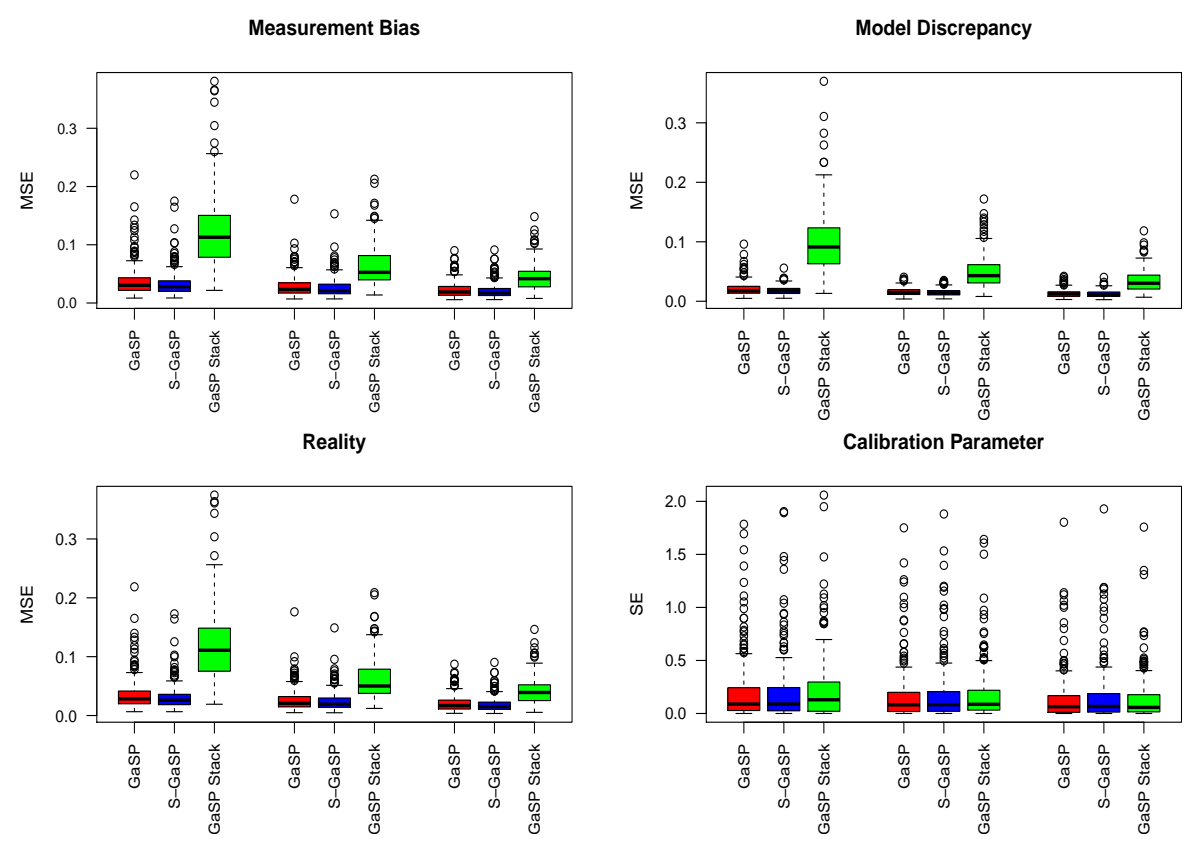


Figure 4: MSE of measurement bias discrepancy function, reality and SE of the calibration parameters for Example 3. In each panel, the first three boxes, the middle three boxes and the right three boxes are the results when k=5, k=10 and k=15, respectively. The MSE of GaSP calibration, S-GaSP calibration based on the full data and the GaSP calibration based on the aggregated data are colored as the red, blue and green.

SEs of the calibration parameter is small when the number of sources of the observations increases, because of the relatively large variance and correlation in the measurement bias. The estimated measurement bias, the model discrepancy reality and their estimations in the first simulated experiment of Example 3 is graphed in supplementary materials. Also included in more simulated data analysis, which shows the variance of MLE for the calibration parameters does not go to zero when the number of sources and number of observations in each source both go to infinity, similar to the result found in Lemma 2.

Example 3 indicates that we are able to separate the measurement bias and model discrepancy functions based on multiple sources of data under certain tolerance bound, when the underlying discrepancy function is sampled from a GaSP. The S-GaSP calibration performs

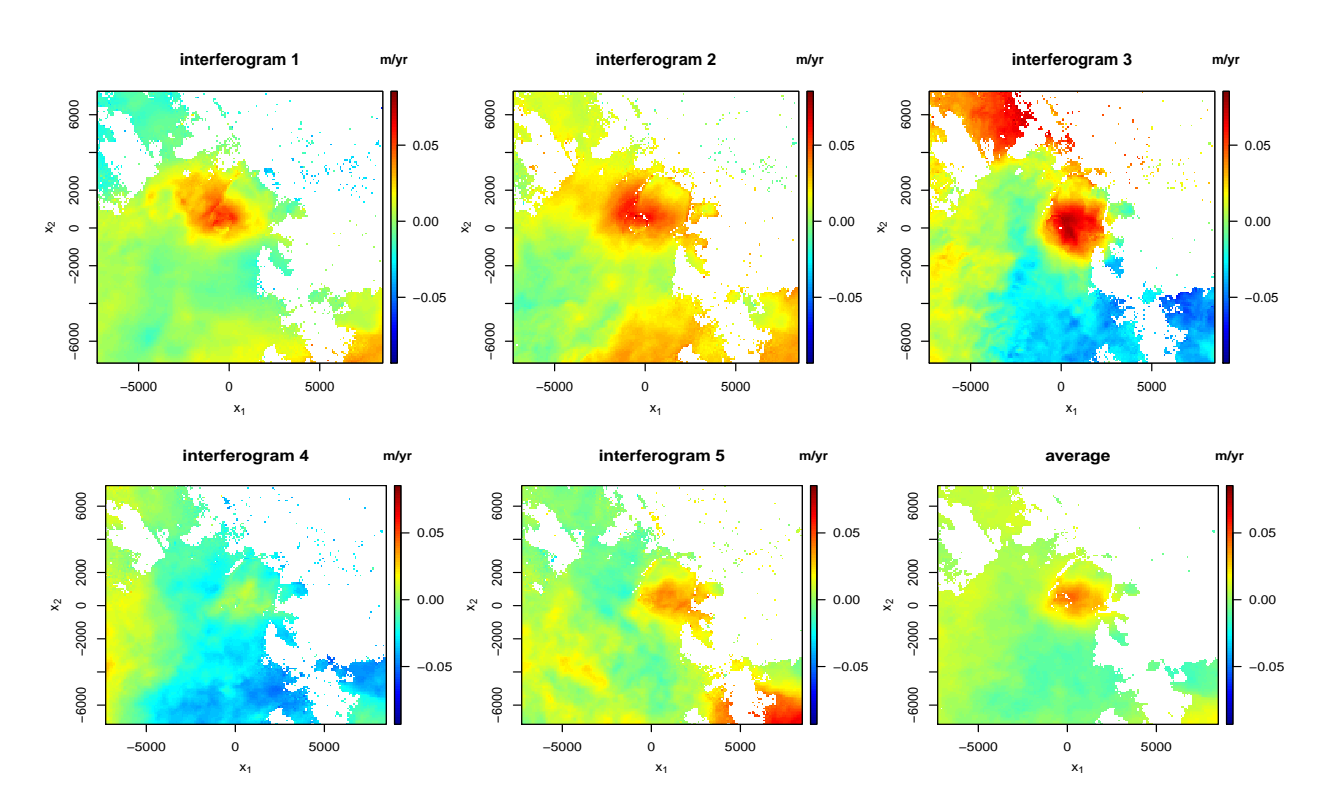


Figure 5: Five COSMO-SkyMed satellite interferograms spanning the following time periods: 1) 17 Oct 2011 - 04 May 2012; 2) 21 Oct 2011 - 16 May 2012; 3); 20 Oct 2011 to 15 May 2012; 4) 28 Oct 2011 to 11 May 2012; 5) 12 Oct 2011 - 07 May 2012. Interferograms 1 and 2 have an ascending-mode look angle, while the rest are descending-mode. Horizontal position is in meters relative to a chosen point in Kīlauea caldera; vertical scale is m/yr. The last figure shows the stack (average) of 6 images.

relatively well, even if the true discrepancy function is sampled from a GaSP.

## 5.2 Geophysical model calibration by InSAR interferograms

In this section, we study the performance of the aforementioned approaches in calibrating the geophysical model of Kīlauea Volcano. Consistent with past work, we hypothesize that our InSAR data can be explained to first-order by a simple geophysical model of volume change of a spherical magma reservoir embedded in an elastic medium (Mogi, 1958; Anderson and Poland, 2016). This model is parameterized entirely by the 3D location of its centroid (east distance, north distance, and depth), its volume change, and the Poisson's ratio of the elastic medium (Table 1).

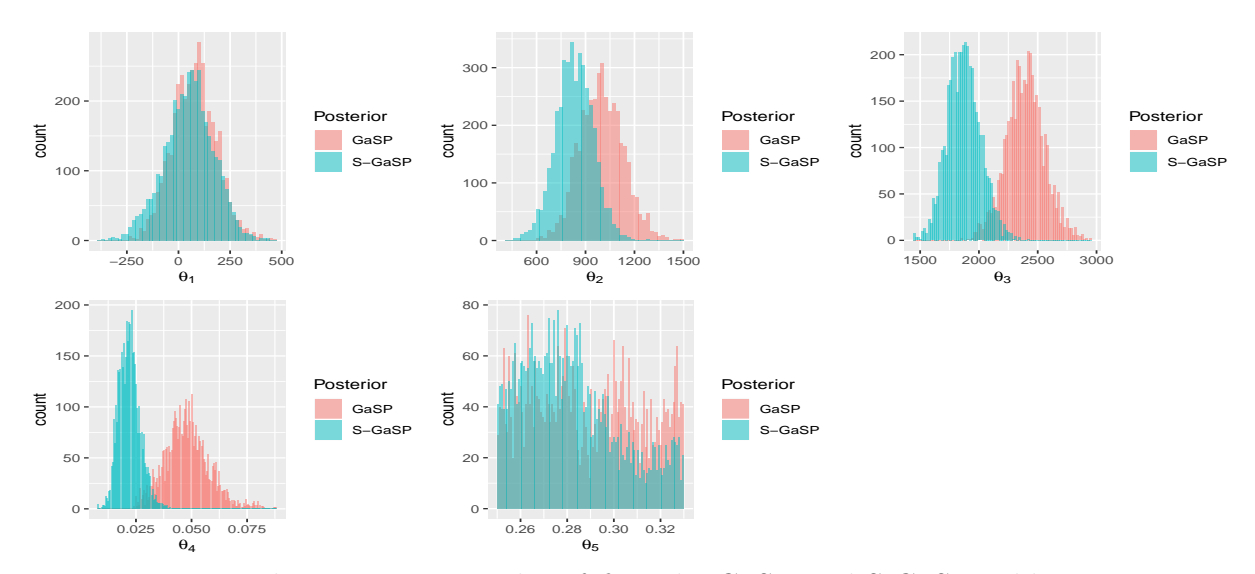


Figure 6: The posterior samples of  $\theta$  in the GaSP and S-GaSP calibrations.

Ground deformation velocities computed from five interferograms captured by the COSMO-SkyMed satellite spanning late 2011 to mid-2012 are shown in Figure 5 (in our model the rate of ground deformation is assumed constant over the complete time range). We first compare the GaSP and S-GaSP calibrations based on observations at 400 uniformly sampled pixels. The parameters of the GaSP and S-GaSP calibrations are given in Table 1. 50,000 posterior samples are drawn with the first 10,000 posterior samples used as the burn-in samples in both models. The posterior samples in every 10th step are saved to reduce storage space and autocorrelation in the Markov Chain.

Figure 6 graphs posterior samples of model calibration parameters. When the discrepancy function is modeled by GaSP, estimates of the chamber depth  $(\theta_3)$  and volume change rate  $(\theta_4)$  are both larger than those of the S-GaSP calibration. This phenomenon was also found in Gu and Wang (2018), which used only two interferograms for calibration. Here we use five interferograms and the measurement bias is modeled. Consequently, the posterior samples of the GaSP and S-GaSP calibrations become closer than the results using two interferograms without modeling the measurement bias.

The MSE of the predictions on each interferogram based on 400 uniformly sampled pixels are given in Table 3. The mean parameters  $\mu$  are treated as a part of the geophysical

Table 3: Predictive mean squared error (MSE) in the prediction of the full interferograms by the GaSP and S-GaSP models based on 400 uniformly sampled pixels in each interferogram.  $MSE_{f^M}$  is the MSE using the calibrated geophysical model for prediction and  $MSE_{f^M+\delta+\delta_l}$  is the MSE using the combined calibrated geophysical model, discrepancy function and measurement bias for prediction. The number is by  $10^{-4}$ .

$\overline{\mathrm{MSE}_{f^M}}$	image 1	image 2	image 3	image 4	image 5	image stack
GaSP	1.30	1.71	7.84	4.46	2.04	0.689
S-GaSP	1.21	1.38	7.69	3.49	1.64	0.611
$\overline{\mathrm{MSE}_{f^M+\delta+\delta_l}}$	image 1	image 2	image 3	image 4	image 5	image stack
GaSP	0.115	0.114	0.264	0.136	0.120	0.0324
S- $GaSP$	0.126	0.123	0.258	0.112	0.127	0.0295

model for making predictions. The S-GaSP is designed to have the calibrated geophysical model explain more variability in the observations, and consequently the S-GaSP-calibrated geophysical model is more accurate in prediction (at points not used for calibration) than the GaSP-calibrated model, shown in the first two rows in Table 3. Furthermore, we also explored other pioneering methods, such as LS and  $L_2$  calibration (Tuo and Wu, 2015; Wong et al., 2017). However, convergence of numerical optimization seems to be a challenging issue when there are multiple sources of data. The measurement bias, which is the focus of this work, was not considered in previous methods.

The predictive mean of each interferogram and stack image from the S-GaSP calibration is shown in Figure 7. Predictions are very close to the real interferogram (with around 99% of pixels held out), and performance is better than with the GaSP calibration method (given in the supplementary materials). Estimated measurement bias and model discrepancy for GaSP and S-GaSP calibrations are given in supplementary materials. Detailed comparison between GaSP and S-GaSP, along with the trace plots of all the parameters, are given in the supplementary materials.

Finally, we compare our results with previous work for the Kīlauea Volcano. Two interferograms used in this study (the second and third interferograms shown in Figure 5) were also used for calibrating the same geophysical model as part of a broader geophysical study (Anderson and Poland, 2016), but that work did not consider spatially-correlated noise in

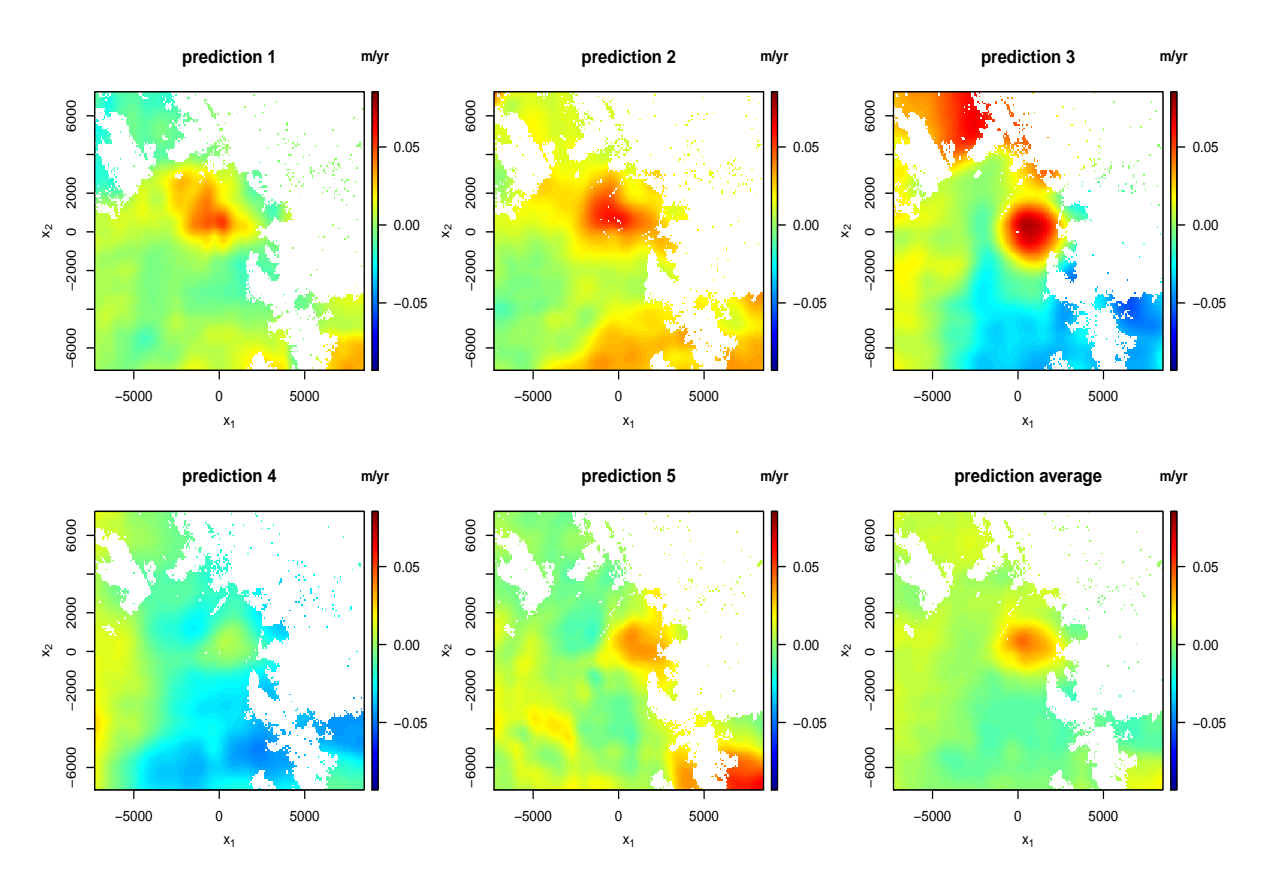


Figure 7: Predictive mean of each interferogram and stack image in S-GaSP calibration.

the data or a discrepancy function. The same two interferograms were used in Gu and Wang (2018) for calibration with a discrepancy function, but the measurement bias in the interferograms was overlooked. Of all the images, the ones used in the previous studies show the largest apparent volcanic ground displacement, and as a result the reservoir volume change rate ( $\theta_4$ ) we estimate here in the S-GaSP calibration using all five images is smaller than in those studies (0.02 m<sup>3</sup>/s vs. 0.04–0.05 m<sup>3</sup>/s, respectively). The results presented in this work are more robust, since more interferograms often better resolve signal from noise.

Estimated reservoir position depends on the spatial pattern of displacements but not the rate. We estimate a reservoir location ~500 m east and ~800 m north of the reference position (SE rim of Halema'uma'u Crater), at 1.9 km depth. Many previous studies have examined reservoir location using a variety of data sets over many years. Despite the relatively low signal-to-noise ratio in the data, our estimated depth is consistent with these studies

(e.g., Poland et al. (2014)). The horizontal position of our most likely reservoir centroid is several hundred meters north of the most commonly-accepted location near the east rim of Halema'uma'u Crater, but is closer than the position estimated previously in Anderson and Poland (2016) and Gu and Wang (2018) using two interferograms without modeling the measurement bias; this confirms the importance of addressing the uncertainty in the measurement bias. Future studies may combine not only multiple measurements of a single type, but also multiple types of data (for instance, GPS or tilt). Furthermore, the number of calibration parameters will be large when a more sophisticated geophysical model is used. Advanced sampling algorithms and design techniques (e.g. Mak et al. (2018)) may be used to represent the posterior distribution.

# 6 Concluding remarks

We have introduced a statistical framework to estimate measurement bias, model discrepancy, and calibration parameters using multiple sources of data. There are several possible future extensions. First of all, the computation based on the full data scales linearly with the number of data sources when the inputs are aligned. When the inputs are misaligned, it will be helpful to design an exact or approximate algorithm for computational purposes. Second, the quadtree-processed images are used widely in downsampling satellite interferograms. A theoretical study on how to model the quadtree images that properly takes into account the size of the boxes and the measurement bias will be very useful. It is also interesting to study whether the quadtree-processed images improve the accuracy in calibration and prediction compared to some alternate designs. Lastly, more work is required to fuse diverse types of data, such as the gas emission, GPS data and InSAR data with geophysical models for data inversion.

#### References

- Anderson, K. and Segall, P. (2011). Physics-based models of ground deformation and extrusion rate at effusively erupting volcanoes. *Journal of Geophysical Research: Solid Earth*, 116(B7).
- Anderson, K. R., Johanson, I. A., Patrick, M. R., Gu, M., Segall, P., Poland, M. P., Montgomery-Brown, E. K., and Miklius, A. (2019). Magma reservoir failure and the onset of caldera collapse at kīlauea volcano in 2018. *Science*, 366(6470).
- Anderson, K. R. and Poland, M. P. (2016). Bayesian estimation of magma supply, storage, and eruption rates using a multiphysical volcano model: Kīlauea volcano, 2000–2012. Earth and Planetary Science Letters, 447:161–171.
- Arendt, P. D., Apley, D. W., and Chen, W. (2012a). Quantification of model uncertainty: Calibration, model discrepancy, and identifiability. *Journal of Mechanical Design*, 134(10):100908.
- Arendt, P. D., Apley, D. W., Chen, W., Lamb, D., and Gorsich, D. (2012b). Improving identifiability in model calibration using multiple responses. *Journal of Mechanical Design*, 134(10):100909.
- Banerjee, S., Carlin, B. P., and Gelfand, A. E. (2014). *Hierarchical modeling and analysis* for spatial data. Crc Press.
- Bayarri, M. J., Berger, J. O., Paulo, R., Sacks, J., Cafeo, J. A., Cavendish, J., Lin, C.-H., and Tu, J. (2007). A framework for validation of computer models. *Technometrics*, 49(2):138–154.
- Biggs, J. and Pritchard, M. E. (2017). Global Volcano Monitoring: What Does It Mean When Volcanoes Deform? *Elements*, 13(1):17–22.

- Bürgmann, R., Rosen, P. A., and Fielding, E. J. (2000). Synthetic Aperture Radar Interferometry to Measure Earth's Surface Topography and Its Deformation. *Annual Review of Earth and Planetary Sciences*, 28(1):169–209.
- Chen, C. W. and Zebker, H. A. (2001). Two-dimensional phase unwrapping with use of statistical models for cost functions in nonlinear optimization. *Journal of the Optical Society of America A*, 18(2):338.
- Gong, W., Lu, Z., and Meyer, F. (2016). Uncertainties in estimating magma source parameters from InSAR observation. In Riley, K., Webley, P., and Thompson, M., editors, *Natural Hazard Uncertainty Assessment: Modeling and Decision Support, Geophysical Monograph* 223, chapter 7, pages 89–104. John Wiley & Sons, Inc.
- Gu, M. (2018). Jointly robust prior for Gaussian stochastic process in emulation, calibration and variable selection. *Bayesian Analysis*, 14(1).
- Gu, M. and Wang, L. (2018). Scaled Gaussian stochastic process for computer model calibration and prediction. SIAM/ASA Journal on Uncertainty Quantification, 6(4):1555–1583.
- Gu, M., Wang, X., and Berger, J. O. (2018a). Robust Gaussian stochastic process emulation.

  Annals of Statistics, 46(6A):3038–3066.
- Gu, M., Xie, F., and Wang, L. (2018b). A theoretical framework of the scaled Gaussian stochastic process in prediction and calibration. arXiv preprint arXiv:1807.03829.
- Guttorp, P. and Gneiting, T. (2006). Studies in the history of probability and statistics xlix on the matern correlation family. *Biometrika*, 93(4):989–995.
- Handcock, M. S. and Stein, M. L. (1993). A Bayesian analysis of Kriging. *Technometrics*, 35(4):403–410.
- Hodges, J. S. and Reich, B. J. (2010). Adding spatially-correlated errors can mess up the fixed effect you love. *The American Statistician*, 64(4):325–334.

- Hooper, A., Segall, P., and Zebker, H. (2007). Persistent Scatterer InSAR for Crustal Deformation Analysis, with Application to Volcan Alcedo, Galapagos. *Journal of Geophysical Research*, 112:1–19.
- Jonsson, S., Zebker, H., Segall, P., and Amelung, F. (2002). Fault Slip Distribution of the 1999 Mw 7.1 Hector Mine, California, Earthquake, Estimated from Satellite Radar and GPS Measurements. *Bulletin of the Seismological Society of America*, 92(4):1377–1389.
- Kennedy, M. C. and O'Hagan, A. (2001). Bayesian calibration of computer models. *Journal* of the Royal Statistical Society: Series B (Statistical Methodology), 63(3):425–464.
- Knospe, S. and Jonsson, S. (2010). Covariance estimation for dinsar surface deformation measurements in the presence of anisotropic atmospheric noise. *IEEE Transactions on Geoscience and Remote Sensing*, 48(4):2057–2065.
- Lim, Y. B., Sacks, J., Studden, W., and Welch, W. J. (2002). Design and analysis of computer experiments when the output is highly correlated over the input space. *Canadian Journal of Statistics*, 30(1):109–126.
- Lohman, R. B. and Simons, M. (2005). Some thoughts on the use of InSAR data to constrain models of surface deformation: Noise structure and data downsampling. *Geochemistry*, *Geophysics*, *Geosystems*, 6(1):n/a–n/a.
- Mak, S., Joseph, V. R., et al. (2018). Support points. Annals of Statistics, 46(6A):2562–2592.
- Massonnet, D., Briole, P., and Arnaud, A. (1995). Deflation of Mount Etna monitored by spaceborne radar interferometry. *Nature*, 375(6532):567–570.
- Mogi, K. (1958). Relations between the eruptions of various volcanoes and the deformations of the ground surfaces around them. *Bull. Earthquake Res. Inst. University of Tokyo*, 36:99–134.

- Montgomery-Brown, E. K., Wicks, C. W., Cervelli, P. F., Langbein, J. O., Svarc, J. L., Shelly, D. R., Hill, D. P., and Lisowski, M. (2015). Renewed inflation of Long Valley Caldera, California (2011 to 2014). *Geophysical Research Letters*, 42(13):5250–5257.
- Neal, C. A., Brantley, S., Antolik, L., Babb, J., Burgess, M., Calles, K., Cappos, M., Chang, J., Conway, S., Desmither, L., et al. (2019). The 2018 rift eruption and summit collapse of kīlauea volcano. *Science*, 363(6425):367–374.
- Nocedal, J. (1980). Updating quasi-newton matrices with limited storage. *Mathematics of computation*, 35(151):773–782.
- Oliver, D. S. and Alfonzo, M. (2018). Calibration of imperfect models to biased observations.

  Computational Geosciences, 22(1):145–161.
- Pinel, V., Poland, M., and Hooper, a. (2014). Volcanology: Lessons learned from Synthetic Aperture Radar imagery. *Journal of Volcanology and Geothermal Research*, 289:81–113.
- Plumlee, M. (2017). Bayesian calibration of inexact computer models. *Journal of the American Statistical Association*, 112(519):1274–1285.
- Poland, M. P., Miklius, A., and Montgomery-Brown, E. K. (2014). Magma Supply, Storage, and Transport at Shield-Stage Hawaiian Volcanoes. In *Characteristics of Hawaiian Volcanoes*, chapter 5, pages 179–234. U.S. Geological Survey Professional Paper 1801.
- Pritchard, M., Simons, M., Rosen, P., Hensley, S., and Webb, F. (2002). Co-seismic slip from the 1995 july 30 m w= 8.1 antofagasta, chile, earthquake as constrained by insar and gps observations. *Geophysical Journal International*, 150(2):362–376.
- Reich, B. J., Hodges, J. S., and Zadnik, V. (2006). Effects of residual smoothing on the posterior of the fixed effects in disease-mapping models. *Biometrics*, 62(4):1197–1206.
- Santner, T. J., Williams, B. J., and Notz, W. I. (2003). The design and analysis of computer experiments. Springer Science & Business Media.

- Simons, M., Fialko, Y., and Rivera, L. (2002). Coseismic deformation from the 1999 Mw 7.1 Hector Mine, California, earthquake as inferred from InSAR and GPS observations.

  Bulletin of the Seismological Society of America, 92(4):1390–1402.
- Simons, M. and Rosen, P. A. (2007). Interferometric synthetic aperture radar geodesy. In *Treatise on Geophysics*, volume 3, pages 391–446. Elsevier Press.
- Stein, M. L. (2012). Interpolation of spatial data: some theory for kriging. Springer Science & Business Media.
- Tuo, R. and Wu, C. J. (2015). Efficient calibration for imperfect computer models. *The Annals of Statistics*, 43(6):2331–2352.
- Tuo, R. and Wu, C. J. (2016). A theoretical framework for calibration in computer models: parametrization, estimation and convergence properties. SIAM/ASA Journal on Uncertainty Quantification, 4(1):767–795.
- Wang, C., Ding, X., Li, Q., and Jiang, M. (2014). Equation-based InSAR data quadtree downsampling for earthquake slip distribution inversion. *IEEE Geoscience and Remote* Sensing Letters, 11(12):2060–2064.
- Wong, R. K., Storlie, C. B., and Lee, T. (2017). A frequentist approach to computer model calibration. *Journal of the Royal Statistical Society: Series B (Statistical Methodology)*, 79:635–648.
- Zebker, H. A., Rosen, P. A., and Hensley, S. (1997). Atmospheric effects in interferometric synthetic aperture radar surface deformation and topographic maps. *Journal of Geophysical Research: Solid Earth*, 102(B4):7547–7563.
- Zhang, H. (2004). Inconsistent estimation and asymptotically equal interpolations in model-based geostatistics. *Journal of the American Statistical Association*, 99(465):250–261.

Supplement of "Calibration of imperfect mathematical models by multiple sources of data with measurement bias"

All the formulas in the supplementary materials are cross-referenced in the main body of the article.

## S1 Proof of Lemma 1

Proof of lemma 1. Note that the likelihood of model for the full data in (3) follows

$$p(\mathbf{y} \mid \boldsymbol{\delta}, \boldsymbol{\theta}, \mu, \sigma_0^2) = (2\pi\sigma_0^2)^{-nk/2} \exp\left(-\frac{\sum_{l=1}^k (\mathbf{y}_l - \boldsymbol{\delta} - \mathbf{f}_\theta - \mu \mathbf{1}_n)^T (\mathbf{y}_l - \boldsymbol{\delta} - \mathbf{f}_\theta - \mu \mathbf{1}_n)}{2\sigma_0^2}\right)$$

$$= (2\pi\sigma_0^2)^{-n(k-1)/2} k^{-n/2} \exp\left(-\frac{\sum_{l=1}^k (\mathbf{y}_l - \bar{\mathbf{y}})^T (\mathbf{y}_l - \bar{\mathbf{y}})}{2\sigma_0^2}\right)$$

$$\times (2\pi\sigma_0^2/k)^{-n/2} \exp\left(-\frac{k(\bar{\mathbf{y}} - \boldsymbol{\delta} - \mathbf{f}_\theta - \mu \mathbf{1}_n)^T (\bar{\mathbf{y}} - \boldsymbol{\delta} - \mathbf{f}_\theta - \mu \mathbf{1}_n)}{2\sigma_0^2}\right)$$

Marginalizing out  $\boldsymbol{\delta}$  based on prior  $\boldsymbol{\delta} \sim \text{MN}(\mathbf{0}, \tau^2 \mathbf{R})$ , we have

$$p(\mathbf{y} \mid \boldsymbol{\theta}, \mu, \sigma_0^2, \tau^2, \mathbf{R})$$

$$= (2\pi\sigma_0^2)^{-n(k-1)/2} k^{-n/2} \exp\left(-\frac{\sum_{l=1}^k (\mathbf{y}_l - \bar{\mathbf{y}})^T (\mathbf{y}_l - \bar{\mathbf{y}})}{2\sigma_0^2}\right)$$

$$\times (2\pi)^{-n/2} \left|\tau^2 \mathbf{R} + \frac{\sigma_0^2}{k} \mathbf{I}_n\right|^{-1/2} \exp\left(-\frac{(\bar{\mathbf{y}} - \mathbf{f}_\theta - \mu \mathbf{1}_n)^T (\tau^2 \mathbf{R} + \frac{\sigma_0^2}{k} \mathbf{I}_n)^{-1} (\bar{\mathbf{y}} - \mathbf{f}_\theta - \mu \mathbf{1}_n)}{2}\right)$$

$$= (2\pi\sigma_0^2)^{-n(k-1)/2} k^{-n/2} \exp\left(-\frac{\sum_{l=1}^k (\mathbf{y}_l - \bar{\mathbf{y}})^T (\mathbf{y}_l - \bar{\mathbf{y}})}{2\sigma_0^2}\right) \bar{p}(\bar{\mathbf{y}} \mid \boldsymbol{\theta}, \mu, \sigma_0^2, \tau^2, \mathbf{R})$$

where  $\bar{p}(\bar{\mathbf{y}} \mid \boldsymbol{\theta}, \mu, \sigma_0^2, \tau^2, \mathbf{R})$  is marginal density of aggregated data after integrating out  $\boldsymbol{\delta}$ , from which we have concluded the proof.

# S2 Marginal distribution and predictive distribution of the multi-calibration model

The observations from the lth source of data are denoted as  $\mathbf{y}_l^F = (y_l^F(\mathbf{x}_1), ..., y_l^F(\mathbf{x}_n))^T$  at  $\{\mathbf{x}_1, ..., \mathbf{x}_n\}$ , for l = 1, ..., k. For the InSAR interferograms, each entry of  $\mathbf{y}_l^F$  represents a line-of-sight displacement at a point on the Earth's surface. The following lemma gives the marginal distribution of model (2), after integrating out the random measurement bias functions.

**Lemma S1.** After integrating out  $\delta_l$  in model (2), l = 1, ..., k, one has the following distributions:

1. For each source l = 1, ..., k, the marginal distribution of the field data follows a multivariate normal distribution

$$(\mathbf{y}_l^F \mid \boldsymbol{\delta}, \boldsymbol{\theta}, \sigma_l^2, \mathbf{R}_l, \mu_l, \sigma_{0l}^2) \sim \text{MN}(\mathbf{f}_{\theta}^M + \mu_l \mathbf{1}_n + \boldsymbol{\delta}, \sigma_l^2 \mathbf{R}_l + \sigma_{0l}^2 \mathbf{I}_n),$$
 (S1)

where  $\mathbf{f}_{\boldsymbol{\theta}}^{M} = (f^{M}(\mathbf{x}_{1}, \boldsymbol{\theta}), ..., f^{M}(\mathbf{x}_{n}, \boldsymbol{\theta}))^{T}$  and  $\boldsymbol{\delta} = (\delta(\mathbf{x}_{1}), ..., \delta(\mathbf{x}_{n}))^{T}$ , with  $\mathbf{I}_{n}$  being an  $n \times n$  identity matrix.

2. The marginal posterior distribution of the discrepancy function follows a multivariate normal distribution

$$(\boldsymbol{\delta} \mid \{y_l^F, \sigma_l^2, \mathbf{R}_l, \sigma_{0l}^2, \mu_l\}_{l=1}^k, \boldsymbol{\theta}, \tau^2, \mathbf{R}) \sim \text{MN}(\hat{\boldsymbol{\delta}}, \hat{\boldsymbol{\Sigma}}),$$
 (S2)

where

$$\hat{\mathbf{\Sigma}} = \left(\sum_{l=1}^{k} \tilde{\mathbf{\Sigma}}_{l}^{-1} + (\tau^{2} \mathbf{R})^{-1}\right)^{-1} \quad and \quad \hat{\boldsymbol{\delta}} = \hat{\mathbf{\Sigma}} \sum_{l=1}^{k} \tilde{\mathbf{\Sigma}}_{l}^{-1} \tilde{\mathbf{y}}_{l},$$

with

$$\tilde{\mathbf{y}}_l = \mathbf{y}_l - \mathbf{f}_{\boldsymbol{\theta}}^M - \mu_l \mathbf{1}_n$$
 and  $\tilde{\mathbf{\Sigma}}_l = \sigma_l^2 \mathbf{R}_l + \sigma_{0l}^2 \mathbf{I}_n$ .

Proof of lemma S1. Marginalizing out  $\delta_l$ , by the laws of the total expectation and total variance, the marginal distribution of  $\mathbf{y}_l^F$  is a multivariate normal distribution with the mean

$$\begin{split} \mathbb{E}[\mathbf{y}_l^F \mid \boldsymbol{\delta}, \, \boldsymbol{\theta}, \, \sigma_l^2, \mathbf{R}_l, \, \mu_l, \, \sigma_{0l}^2] = & \mathbb{E}[\mathbb{E}[\mathbf{y}_l^F \mid \boldsymbol{\delta}, \, \boldsymbol{\theta}, \, \sigma_l^2, \mathbf{R}_l, \, \mu_l, \, \sigma_{0l}^2, \, \boldsymbol{\delta}_l]] \\ = & \mathbb{E}[\mathbf{f}_{\boldsymbol{\theta}}^M + \mu_l \mathbf{1}_n + \boldsymbol{\delta} + \boldsymbol{\delta}_l \mid \boldsymbol{\delta}, \, \boldsymbol{\theta}, \, \sigma_l^2, \mathbf{R}_l, \, \mu_l, \, \sigma_{0l}^2] \\ = & \mathbf{f}_{\boldsymbol{\theta}}^M + \mu_l \mathbf{1}_n + \boldsymbol{\delta}, \end{split}$$

and the covariance matrix

$$V[\mathbf{y}_{l}^{F} \mid \boldsymbol{\delta}, \boldsymbol{\theta}, \sigma_{l}^{2}, \mathbf{R}_{l}, \mu_{l}, \sigma_{0l}^{2}]$$

$$= V[\mathbb{E}[\mathbf{y}_{l}^{F} \mid \boldsymbol{\delta}, \boldsymbol{\theta}, \sigma_{l}^{2}, \mathbf{R}_{l}, \mu_{l}, \sigma_{0l}^{2}, \boldsymbol{\delta}_{l}]] + \mathbb{E}[V[\mathbf{y}_{l}^{F} \mid \boldsymbol{\delta}, \boldsymbol{\theta}, \sigma_{l}^{2}, \mathbf{R}_{l}, \mu_{l}, \sigma_{0l}^{2}, \boldsymbol{\delta}_{l}]]$$

$$= V[\mathbf{f}_{\theta}^{M} + \mu_{l} \mathbf{1}_{n} + \boldsymbol{\delta} + \boldsymbol{\delta}_{l} \mid \boldsymbol{\delta}, \boldsymbol{\theta}, \sigma_{l}^{2}, \mathbf{R}_{l}, \mu_{l}, \sigma_{0l}^{2}] + \sigma_{0l}^{2} \mathbf{I}_{n}$$

$$= \sigma_{l}^{2} \mathbf{R}_{l} + \sigma_{0l}^{2} \mathbf{I}_{n},$$

from which (S1) follows.

After marginalizing out  $\{\boldsymbol{\delta}_l\}_{l=1}^k$ , the posterior distribution of  $\boldsymbol{\delta}$  follows a multivariate normal distribution with the mean and covariance matrix given in (S2), from which the proof is complete.

Further marginalizing out  $\boldsymbol{\delta}$ , the marginal distribution of the field data  $\mathbf{Y}_v^F := ((\mathbf{y}_1^F)^T, ..., (\mathbf{y}_k^F)^T)^T$  is given in the following lemma.

**Lemma S2.** After integrating out both  $\delta$  and  $\delta_l$ , l = 1, ..., k, the marginal distribution of the field data follows a multivariate normal distribution

$$(\mathbf{Y}_{v}^{F} \mid \{\sigma_{l}^{2}, \mathbf{R}_{l}, \sigma_{0l}^{2}, \mu_{l}\}_{l=1}^{k}, \boldsymbol{\theta}, \tau^{2}, \mathbf{R}) \sim \text{MN}(\mathbf{1}_{k} \otimes \mathbf{f}_{\boldsymbol{\theta}}^{M} + \boldsymbol{\mu} \otimes \mathbf{1}_{n}^{T}, \tau^{2} \mathbf{1}_{k} \mathbf{1}_{k}^{T} \otimes \mathbf{R} + \boldsymbol{\Lambda}),$$
 (S3)

where  $\otimes$  denotes the Kronecker product,  $\boldsymbol{\mu} = (\mu_1, ..., \mu_k)^T$  and  $\boldsymbol{\Lambda}$  is a  $kn \times kn$  block diagonal matrix, with the 1th diagonal block being  $\tilde{\boldsymbol{\Sigma}}_l$  defined in Lemma S1, l = 1, ..., k. The density of (S3) can be expressed as

$$p\left(\mathbf{Y}_{v}^{F} \mid \{\sigma_{l}^{2}, \mathbf{R}_{l}, \sigma_{0l}^{2}, \mu_{l}\}_{l=1}^{k}, \boldsymbol{\theta}, \tau^{2}, \mathbf{R}\right)$$

$$= (2\pi)^{-\frac{nk}{2}} \tau^{-n} |\mathbf{R}|^{-\frac{1}{2}} |\hat{\boldsymbol{\Sigma}}|^{\frac{1}{2}} \prod_{l=1}^{k} |\tilde{\boldsymbol{\Sigma}}_{l}|^{-\frac{1}{2}}$$

$$\times \exp\left\{-\frac{1}{2} \left(\sum_{l=1}^{k} \tilde{\mathbf{y}}_{l}^{T} \tilde{\boldsymbol{\Sigma}}_{l}^{-1} \tilde{\mathbf{y}}_{l} - (\sum_{l=1}^{k} \tilde{\boldsymbol{\Sigma}}_{l}^{-1} \tilde{\mathbf{y}}_{l})^{T} \hat{\boldsymbol{\Sigma}}^{-1} (\sum_{l=1}^{k} \tilde{\boldsymbol{\Sigma}}_{l}^{-1} \tilde{\mathbf{y}}_{l})\right)\right\},$$
(S4)

where  $\hat{\Sigma}$ ,  $\tilde{\mathbf{y}}_l$ , and  $\tilde{\Sigma}_l$  are defined in Lemma S1, for l = 1, ..., k.

Proof of Lemma S2. After marginalizing out  $\delta_l$ , l = 1, ..., k, one has

$$(\mathbf{Y}_v^F \mid \{\sigma_l^2, \mathbf{R}_l, \sigma_{0l}^2, \mu_l\}_{l=1}^k, \boldsymbol{\delta}, \boldsymbol{\theta}, \tau^2, \mathbf{R}) \sim \text{MN}(\mathbf{1}_k \otimes \mathbf{f}_{\theta}^M + \boldsymbol{\mu} \otimes \mathbf{1}_n + \mathbf{1}_k \otimes \boldsymbol{\delta}, \boldsymbol{\Lambda}),$$
 (S5)

where  $\Lambda$  is a block diagonal matrix with the lth diagonal block being  $\tilde{\Sigma}_l$ , l=1,...,k.

Note  $(\boldsymbol{\delta} \mid \tau^2, \mathbf{R}) \sim \text{MN}(\mathbf{0}, \tau^2 \mathbf{R})$ . Further marginalizing out  $\boldsymbol{\delta}$ , the marginal distribution of  $(\mathbf{Y}^F \mid \{\sigma_l^2, \mathbf{R}_l, \sigma_{0l}^2, \mu_l\}_{l=1}^k, \boldsymbol{\theta}, \tau^2, \mathbf{R})$  follows a multivariate normal distribution, with the mean

$$\mathbb{E}[\mathbf{Y}_v^F \mid \{\sigma_l^2, \mathbf{R}_l, \sigma_{0l}^2, \mu_l\}_{l=1}^k, \boldsymbol{\theta}, \tau^2, \mathbf{R}] = \mathbb{E}[\mathbb{E}[\mathbf{Y}_v^F \mid \{\sigma_l^2, \mathbf{R}_l, \sigma_{0l}^2, \mu_l\}_{l=1}^k, \boldsymbol{\delta}, \boldsymbol{\theta}, \tau^2, \mathbf{R}]]$$
$$= \mathbf{1}_k \otimes \mathbf{f}_{\theta}^M,$$

and the posterior variance

$$\begin{split} & \mathbb{V}[\mathbf{Y}_{v}^{F} \mid \{\sigma_{l}^{2}, \mathbf{R}_{l}, \sigma_{0l}^{2}, \mu_{l}\}_{l=1}^{k}, \boldsymbol{\theta}, \tau^{2}, \mathbf{R}] \\ &= \mathbb{V}[\mathbb{E}[\mathbf{Y}_{v}^{F} \mid \{y_{l}^{F}, \tilde{\boldsymbol{\Sigma}}_{l}, \mu_{l}\}_{l=1}^{k}, \boldsymbol{\delta}, \boldsymbol{\theta}, \tau^{2}, \mathbf{R}]] + \mathbb{E}[\mathbb{V}[\mathbf{Y}_{v}^{F} \mid \{y_{l}^{F}, \tilde{\boldsymbol{\Sigma}}_{l}, \mu_{l}\}_{l=1}^{k}, \boldsymbol{\delta}, \boldsymbol{\theta}, \tau^{2}, \mathbf{R}]] \\ &= \mathbb{V}[\mathbf{1}_{k} \otimes \mathbf{f}_{\theta}^{M} + \boldsymbol{\mu} \otimes \mathbf{1}_{n} + \mathbf{1}_{k} \otimes \boldsymbol{\delta} \mid \{\sigma_{l}^{2}, \mathbf{R}_{l}, \sigma_{0l}^{2}, \mu_{l}\}_{l=1}^{k}, \boldsymbol{\theta}, \tau^{2}, \mathbf{R}] + \boldsymbol{\Lambda} \\ &= \mathbf{1}_{k} \mathbf{1}_{k}^{T} \otimes (\tau^{2} \mathbf{R}) + \boldsymbol{\Lambda}, \end{split}$$

from which (S3) follows. Note that the density of  $(\mathbf{Y}_v^F, \boldsymbol{\delta})$  follows

$$p\left(\mathbf{Y}_{v}^{F}, \boldsymbol{\delta} \mid \{\sigma_{l}^{2}, \mathbf{R}_{l}, \sigma_{0l}^{2}, \mu_{l}\}_{l=1}^{k}, \boldsymbol{\theta}, \tau^{2}, \mathbf{R}\right)$$

$$= \prod_{l=1}^{k} \left\{ (2\pi)^{-\frac{n}{2}} |\tilde{\boldsymbol{\Sigma}}_{l}|^{-\frac{1}{2}} \exp\left(-\frac{(\tilde{\mathbf{y}}_{l} - \boldsymbol{\delta})^{T} \tilde{\boldsymbol{\Sigma}}_{l}^{-1} (\tilde{\mathbf{y}}_{l} - \boldsymbol{\delta})}{2}\right) \right\}$$

$$\times (2\pi\tau^{2})^{-\frac{n}{2}} |\mathbf{R}|^{-\frac{1}{2}} \exp\left(-\frac{\boldsymbol{\delta}^{T} \mathbf{R}^{-1} \boldsymbol{\delta}}{2\tau^{2}}\right).$$

Directly marginalizing out  $\boldsymbol{\delta}$  from the above equation yields the density of  $(\mathbf{Y}_v^F \mid \{\sigma_l^2, \mathbf{R}_l, \sigma_{0l}^2, \mu_l\}_{l=1}^k, \boldsymbol{\theta}, \tau^2, \mathbf{R})$ 

Both Lemma S1 and Lemma S2 can be used for computing the likelihood given the other parameters in the full Bayesian analysis. Lemma S2 may be used to develop the maximum likelihood estimator, as both the random model discrepancy and measurement bias functions are marginalized out explicitly. Note that the computational complexity of the marginal density of the field data is  $O((k+1)n^3)$  in both lemmas, for inverting k+1 covariance matrices, each with the size  $n \times n$ , rather than  $O((kn)^3)$ , even if the covariance matrix in (S3) is  $nk \times nk$  in Lemma S2. Such simplification is the key to proceed without approximations to compute the likelihood, if n is not very large. Note that the simplifications of computation rely on the aligned measurements of each source of field data. When the measurements are misaligned, approximations might be needed when the number of sources is large.

Since the discrepancy function between the mathematical model and reality is often scientifically important, one can draw and record  $\delta$  using Lemma S1 in the posterior sampling. The following theorem gives the predictive distribution at any input  $\mathbf{x}$ , given the parameters and posterior samples of  $\delta$ .

**Theorem S1.** For any  $\mathbf{x}^* \in \mathcal{X}$ , one has the following predictive distributions for model (2):

1. The predictive distribution of model discrepancy at any input  $\mathbf{x}^*$  follows a normal distribution

$$(\delta(\mathbf{x}^*) \mid \boldsymbol{\delta}, \{\mathbf{y}_l^F, \sigma_l^2, K_l(\cdot, \cdot), \sigma_{0l}^2, \mu_l\}_{l=1}^k, \boldsymbol{\theta}, \tau^2, K(\cdot, \cdot)) \sim N(\hat{\delta}(\mathbf{x}^*), \tau^2 \hat{K}^{**}),$$

where 
$$\hat{\delta}(\mathbf{x}^*) = \mathbf{r}(\mathbf{x}^*)^T \mathbf{R}^{-1} \boldsymbol{\delta}$$
,  $\mathbf{r}(\mathbf{x}^*) = (K(\mathbf{x}^*, \mathbf{x}_1), ..., K(\mathbf{x}^*, \mathbf{x}_n))^T$ , and  $\hat{K}^{**} = K(\mathbf{x}^*, \mathbf{x}^*) - \mathbf{r}(\mathbf{x}^*)^T \mathbf{R}^{-1} \mathbf{r}(\mathbf{x}^*)$ .

2. For each source l, l = 1,...,k, the predictive distribution of the measurement bias at any input  $\mathbf{x}^*$  follows a normal distribution

$$(\delta_l(\mathbf{x}^*) \mid \boldsymbol{\delta}, \{\mathbf{y}_l^F, \sigma_l^2, K_l(\cdot, \cdot), \sigma_{0l}^2, \mu_l\}_{l=1}^k, \boldsymbol{\theta}, \tau^2, K(\cdot, \cdot)) \sim N(\hat{\delta}_l(\mathbf{x}^*), \sigma_l^2 \hat{K}_l^{**}),$$

where  $\hat{\delta}_l(\mathbf{x}^*) = \sigma_l^2 r_l(\mathbf{x}^*)^T \tilde{\Sigma}_l^{-1} (\tilde{\mathbf{y}}_l^F - \boldsymbol{\delta})$  and  $\hat{K}_l^{**} = K_l(\mathbf{x}^*, \mathbf{x}^*) - \sigma_l^2 \mathbf{r}_l(\mathbf{x}^*)^T \tilde{\Sigma}_l^{-1} \mathbf{r}_l(\mathbf{x}^*),$  with  $\mathbf{r}_l(\mathbf{x}^*) = (K_l(\mathbf{x}^*, \mathbf{x}_1), ..., K_l(\mathbf{x}^*, \mathbf{x}_n))^T$ ,  $\tilde{\mathbf{y}}_l^F$  and  $\tilde{\Sigma}_l^{-1}$  being defined in Lemma S1, for l = 1, ..., k.

3. For each source l, l = 1, ..., k, the predictive distribution of the field data at any input  $\mathbf{x}^*$  follows a normal distribution

$$(y_l^F(\mathbf{x}^*) \mid \boldsymbol{\delta}, \{\mathbf{y}_l^F, \sigma_l^2, K_l(\cdot, \cdot), \sigma_{0l}^2, \mu_l\}_{l=1}^k, \boldsymbol{\theta}, \tau^2, K(\cdot, \cdot))$$
  
  $\sim N(\hat{y}_l^F(\mathbf{x}^*), \tau^2 \hat{K}^{**} + \sigma_l^2 \hat{K}_l^{**} + \sigma_{0l}^2),$ 

where 
$$\hat{y}_l^F(\mathbf{x}^*) = \hat{\delta}(\mathbf{x}^*) + \hat{\delta}_l(\mathbf{x}^*) + f^M(\mathbf{x}^*, \boldsymbol{\theta}) + \mu_l$$
.

*Proof of Theorem S1.* We only verify the third claim and the previous two claims can be verified similarly. For the third claim, the mean follows

$$\mathbb{E}\left[\mathbf{y}_{l}^{F}(\mathbf{x}^{*}) \mid \boldsymbol{\delta}, \{\mathbf{y}_{l}^{F}, \sigma_{l}^{2}, K_{l}(\cdot, \cdot), \sigma_{0l}^{2}, \mu_{l}\}_{l=1}^{k}, \boldsymbol{\theta}, \tau^{2}, K(\cdot, \cdot)\right]$$

$$= \mathbb{E}\left[\delta(\mathbf{x}^{*}) + \delta_{l}(\mathbf{x}^{*}) + f^{M}(\mathbf{x}^{*}.\boldsymbol{\theta}) + \mu_{l} \mid \boldsymbol{\delta}, \{\mathbf{y}_{l}^{F}, \sigma_{l}^{2}, K_{l}(\cdot, \cdot), \sigma_{0l}^{2}, \mu_{l}\}_{l=1}^{k}, \boldsymbol{\theta}, \tau^{2}, K(\cdot, \cdot)\right]$$

$$= \mathbf{r}(\mathbf{x}^{*})^{T} \mathbf{R}^{-1} \boldsymbol{\delta} + \sigma_{l}^{2} \mathbf{r}_{l}(\mathbf{x}^{*}) \tilde{\boldsymbol{\Sigma}}_{l}^{-1}(\mathbf{y}_{l}^{F} - \mathbf{f}_{\boldsymbol{\theta}}^{M} - \mu_{l} \mathbf{1}_{n} - \boldsymbol{\delta}) + f^{M}(\mathbf{x}^{*}, \boldsymbol{\theta}) + \mu_{l}$$

$$= \hat{\delta}(\mathbf{x}^{*}) + \hat{\delta}_{l}(\mathbf{x}^{*}) + f^{M}(\mathbf{x}^{*}, \boldsymbol{\theta}) + \mu_{l},$$

and the variance is

$$\mathbb{V}\left[\mathbf{y}_{l}^{F}(\mathbf{x}^{*}) \mid \boldsymbol{\delta}, \{\mathbf{y}_{l}^{F}, \sigma_{l}^{2}, K_{l}(\cdot, \cdot), \sigma_{0l}^{2}, \mu_{l}\}_{l=1}^{k}, \boldsymbol{\theta}, \tau^{2}, K(\cdot, \cdot)\right] \\
= \mathbb{V}\left[\mathbb{E}\left[\mathbf{y}_{l}^{F}(\mathbf{x}^{*}) \mid \boldsymbol{\delta}, \{\mathbf{y}_{l}^{F}, \sigma_{l}^{2}, K_{l}(\cdot, \cdot), \sigma_{0l}^{2}, \mu_{l}\}_{l=1}^{k}, \boldsymbol{\theta}, \tau^{2}, K(\cdot, \cdot), \delta(\mathbf{x}^{*}), \delta_{l}(\mathbf{x}^{*})\right]\right] + \sigma_{l0}^{2} \\
= \mathbb{V}\left[\delta(\mathbf{x}^{*}) + \delta_{l}(\mathbf{x}^{*}) + f^{M}(\mathbf{x}^{*}, \boldsymbol{\theta}) + \mu_{l} \mid \boldsymbol{\delta}, \mathbf{y}_{l}^{F}, \sigma_{l}^{2}, K_{l}(\cdot, \cdot), \sigma_{0l}^{2}, \mu_{l}, \boldsymbol{\theta}, \tau^{2}, K(\cdot, \cdot)\right] + \sigma_{l0}^{2} \\
= \tau^{2} \hat{K}^{**} + \sigma_{l}^{2} \hat{K}_{l}^{**} + \sigma_{l0}^{2}.$$

The claim soon follows by noticing the predictive distribution is a multivariate normal distribution.

## S3 Proof of Lemma 2

Proof of Lemma 2. First by equation (5), as the sampling model is (3), the MLE of the calibration parameter is the same as using the full data or the aggregated data  $\bar{\mathbf{y}}^F$ . Based on the limiting distribution of the aggregated data in equation (6), when  $k \to \infty$ , the MLE of the calibration parameter is  $\hat{\theta}_{MLE} = (\mathbf{1}_n^T \mathbf{R}^{-1} \mathbf{1}_n)^{-1} \mathbf{1}_n^T \mathbf{R}^{-1} \bar{\mathbf{y}}^F$  with the sampling distribution

$$\hat{\theta}_{MLE} \sim N(\theta, \tau^2 (\mathbf{1}_n^T \mathbf{R}^{-1} \mathbf{1}_n)^{-1}).$$

Denote  $\rho_n = \exp(-\frac{1}{n\gamma})$ . The inverse correlation matrix can be computed explicitly Gu

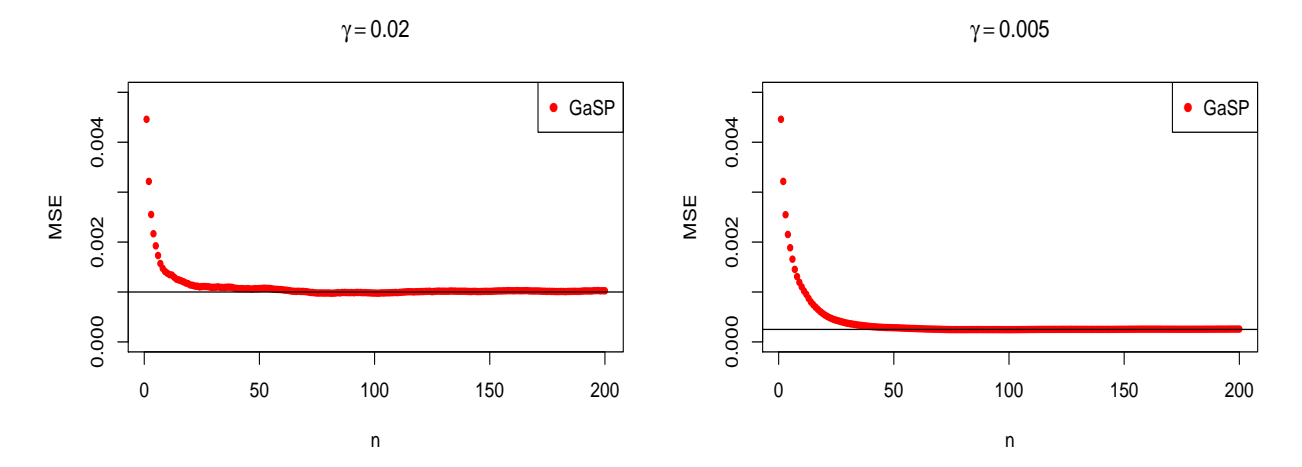


Figure S1: The MSEs of the maximum likelihood estimator of the calibration parameter in Example 3 at different n when  $k \to \infty$  with  $\gamma = 0.02$  and  $\gamma = 0.005$  are graphed in the left panel and right panel, respectively. The black lines are 0.001 and 0.00025 in the left panel and right panel, respectively.

et al. (2018a)

$$\mathbf{R}^{-1} = \frac{1}{1 - \rho_n^2} \begin{pmatrix} 1 & -\rho_n & 0 & 0 & \dots & 0 \\ -\rho_n & 1 + \rho_n^2 & -\rho_n & 0 & \dots & 0 \\ 0 & -\rho_n & 1 + \rho_n^2 & -\rho_n & \dots & 0 \\ \vdots & \vdots & \vdots & \ddots & \vdots & \vdots \\ 0 & 0 & \dots & -\rho_n & 1 + \rho_n^2 & -\rho_n \\ 0 & 0 & \dots & 0 & -\rho_n & 1 \end{pmatrix}.$$

When  $n \to \infty$ , the variance of the sampling distribution of  $\hat{\theta}_{MLE}$  is

$$\mathbb{V}[\theta_{MLE}] = \lim_{n \to \infty} \tau^2 (\mathbf{1}_n^T \mathbf{R}^{-1} \mathbf{1}_n)^{-1}$$

$$= \lim_{n \to \infty} \tau^2 \frac{1 - \exp(-\frac{2}{n\gamma})}{(1 - \exp(-\frac{1}{n\gamma}))(n - (n-2)\exp(-\frac{1}{n\gamma}))}$$

$$= \frac{2\tau^2 \gamma}{2\gamma + 1},$$

where the last line follows from the Taylor expansion. This completes the proof.

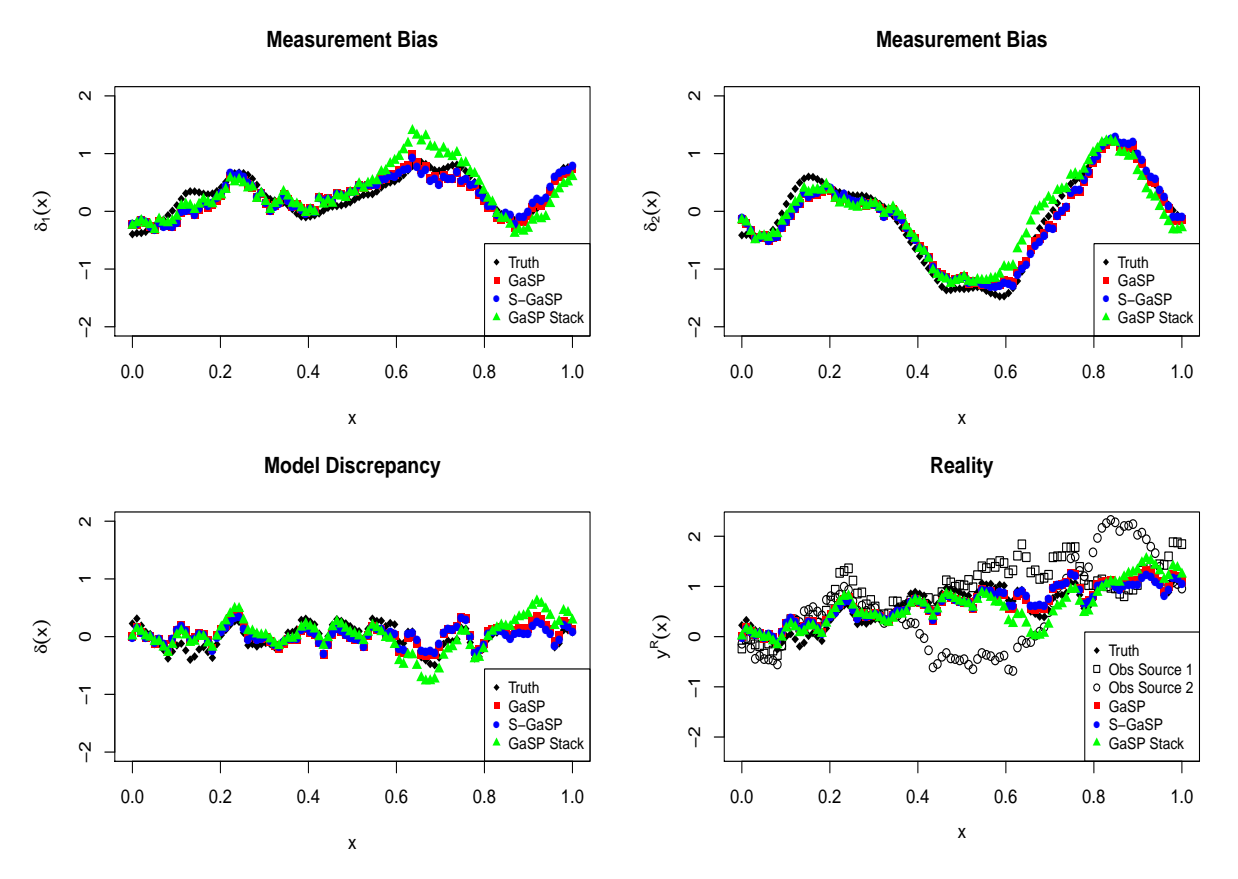


Figure S2: The measurement bias in the first two sources, the model discrepancy function and the reality in the first experiment of Example 3 when k=10 are graphed in the upper panels, lower left panel and lower right panel, respectively. The truth, the estimation by the GaSP and S-GaSP calibrations based on the full data are graphed as the black diamonds, the red squares and blue dots, respectively. The estimation of the GaSP calibration based on aggregated data, denoted as GaSP Stack, is graphed as the green triangles. The observations from the first two sources are graphed as black squares and circles, respectively, in the lower right panel. The black diamonds, red squares and blue dots almost overlap in all panels.

# S4 Additional results for Example 3

We graphed the measurement bias, the model discrepancy reality and their estimations in the first simulated experiment of Example 3 with k = 10 in Figure S2. All methods seem to capture the patterns of the measurement bias, model discrepancy and reality. The estimation by the GaSP and S-GaSP calibrations based on the full data are more accurate than the GaSP calibration using the aggregated data. This is because the true model contains the measurement bias and unknown variance of the noise. The inference based on the full data

is thus more precise in this scenario.

When the number of sources of the data goes to infinity, the limiting distribution based on the aggregated data in Example 3 is given in equation (6). We sample the data from the limiting distribution and compute the maximum likelihood estimator of the calibration parameter at different sample sizes. We repeat 500 experiments and graph the average MSE of the MLE of the calibration parameter in Figure S1. Two scenarios are considered with  $\gamma = 0.02$  (the setting assumed in Example 3) and  $\gamma = 0.005$ . Comparing the left panel and the right panel in Figure S1, the average MSE is smaller when  $\gamma$  is smaller because measurement bias at different inputs is less correlated in this scenario. When the sample size increases, the MSE does not decrease to zero in both scenarios. The lower bound of the MSE in the left panel, however, is much smaller than the MSE we obtained using k = 15 sources of data, shown in lower right panel in Figure 4 in the main manuscript. Thus, when more sources of data are available, the estimation of the calibration parameters will typically become more accurate.

# S5 Additional results for real data analysis

We give more results of the real data analysis in this Section. The predictive mean of each interferogram and stack image in GaSP calibration is given in Figure S3. They are also close to the truth, but they have larger predictive error compared to those from S-GaSP.

Estimated measurement bias and model discrepancy for GaSP and S-GaSP calibrations are shown in Figures S4 and S5, respectively. The calibrated computer model by the GaSP and S-GaSP calibration models of the interferograms with measurement bias are shown in Figure S6. The estimated model discrepancy in the GaSP calibration suggests that the calibrated geophysical model may underestimate the ground displacement in the southeast region. However, this is likely caused by the atmospheric artifact appearing in the first, second and fifth panel in Figure 6. In comparison, the atmospheric artifact seems to be

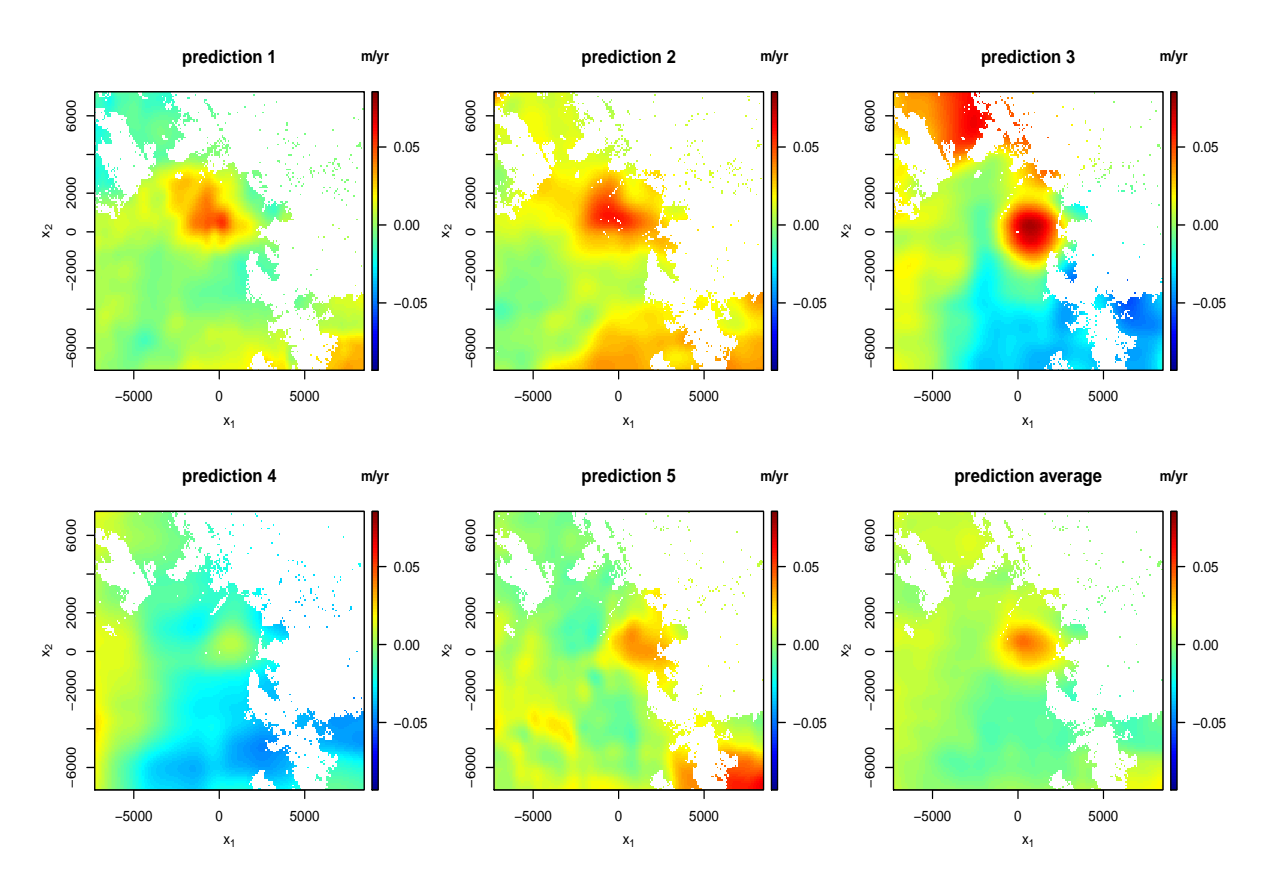


Figure S3: Predictive mean of each interferogram and stack image in GaSP calibration.

properly explained as measurement bias in the S-GaSP calibration shown in Figure S5.

Next, we compare parameter estimates obtained using individual images to those obtained using image stacks. Each of our five interferograms was captured at one of two different look two angles. We construct two stacked images - one for each set of images recorded at each look vector. We compare uniform sampling with the quadtree approach discussed in Section 2.3. The posterior samples of the GaSP and S-GaSP calibrations using stacked images are shown in Figure S7. The posterior calibration parameters of all methods using the stacked images seem to be close to the posterior mean of the calibration parameters in the S-GaSP calibration using the full data plotted as the blue dotted lines in each panel. After averaging different images, the overall range of the ground deformation in the stacked image gets smaller. As the geophysical model with a comparatively shallow magma chamber and smaller storage rate leads to smaller overall change of the ground deformation,

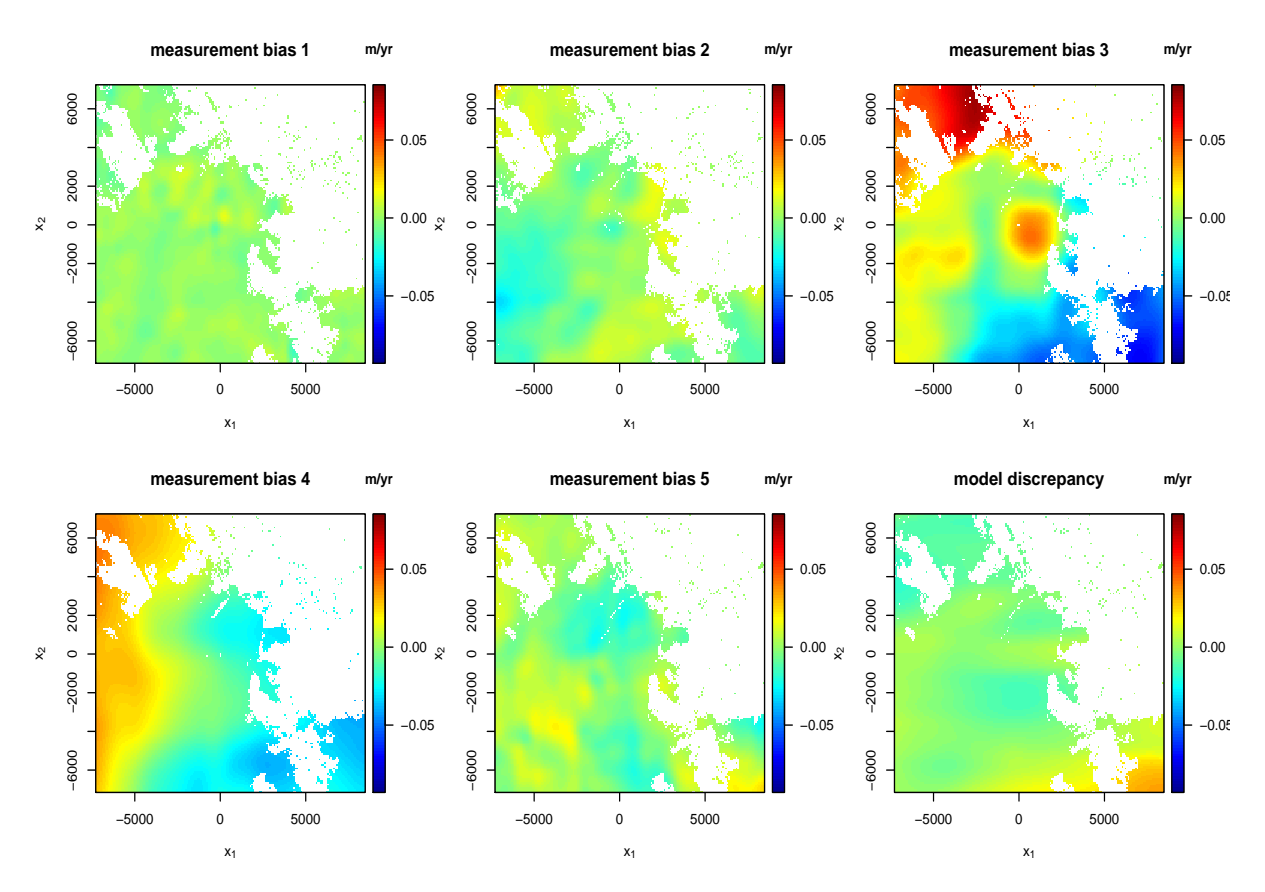


Figure S4: Estimated measurement bias and model discrepancy in the GaSP calibration.

all methods using the stacked images agree with the results by the S-GaSP calibration based on the individual images.

Although stacked images can reduce the measurement bias and noise contained in the observations, one usually loses some information in estimating the measurement bias and discrepancy function using aggregated data. Among all approaches, the S-GaSP calibration based on the full data seems to be both robust in estimating the calibration parameters, and accurate in separating measurement bias and model discrepancy from the observations.

For Figure S8 and Figure S9, the first row and second row are the trace plots of the calibration parameters and mean parameters, respectively. The trace plots of the inverse range parameters of the measurement bias are shown in the third and fourth rows. The fifth row and sixth row show the trace plots of the nugget parameters and scale parameters of the measurement bias, respectively. The last three panels in the last row give the trace plots of

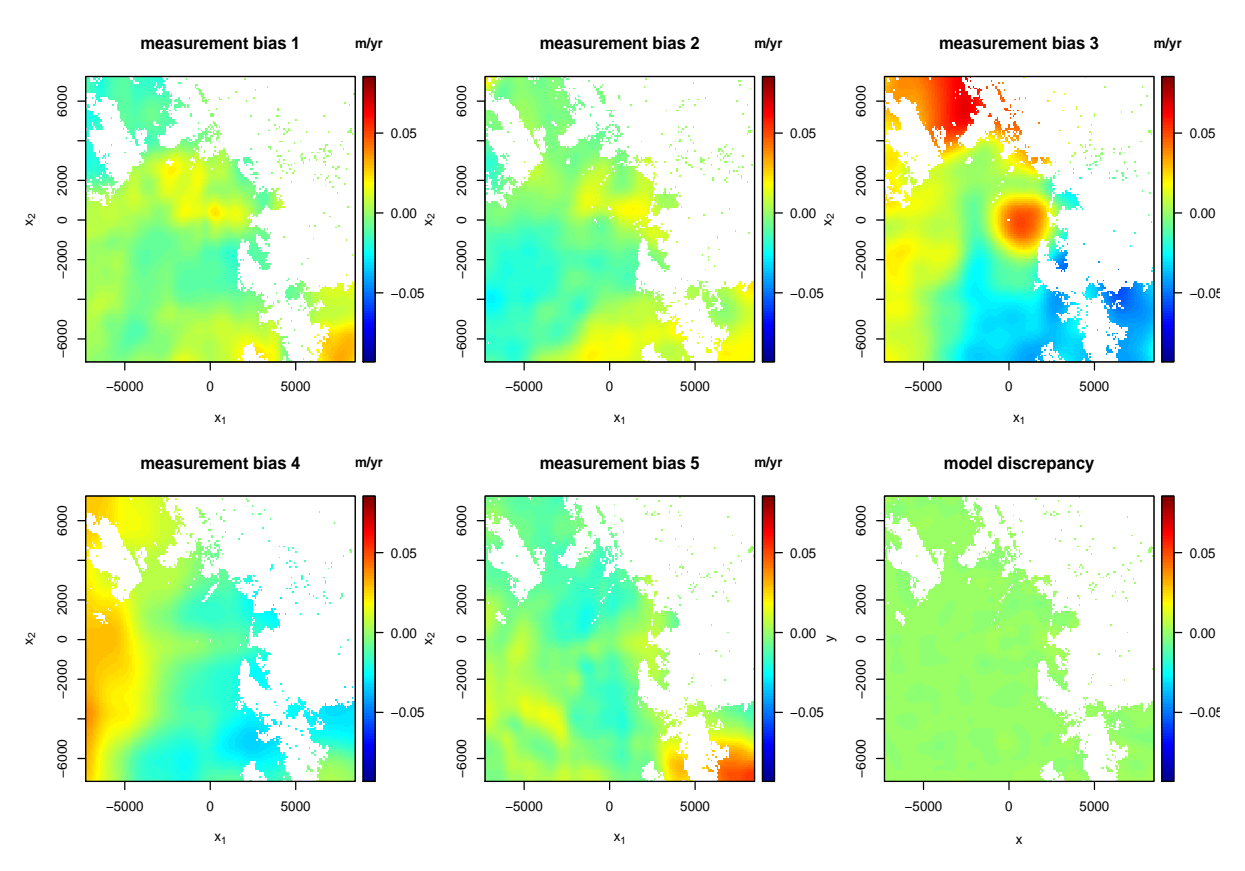


Figure S5: Estimated measurement bias and model discrepancy in the S-GaSP calibration.

the inverse range parameters and the scale parameters in the discrepancy function.

Finally, the trace plots of all the parameters in the GaSP calibration and S-GaSP calibration are given in Figure S8 and Figure S9, respectively. Most of posterior samples seem to mix reasonably well.

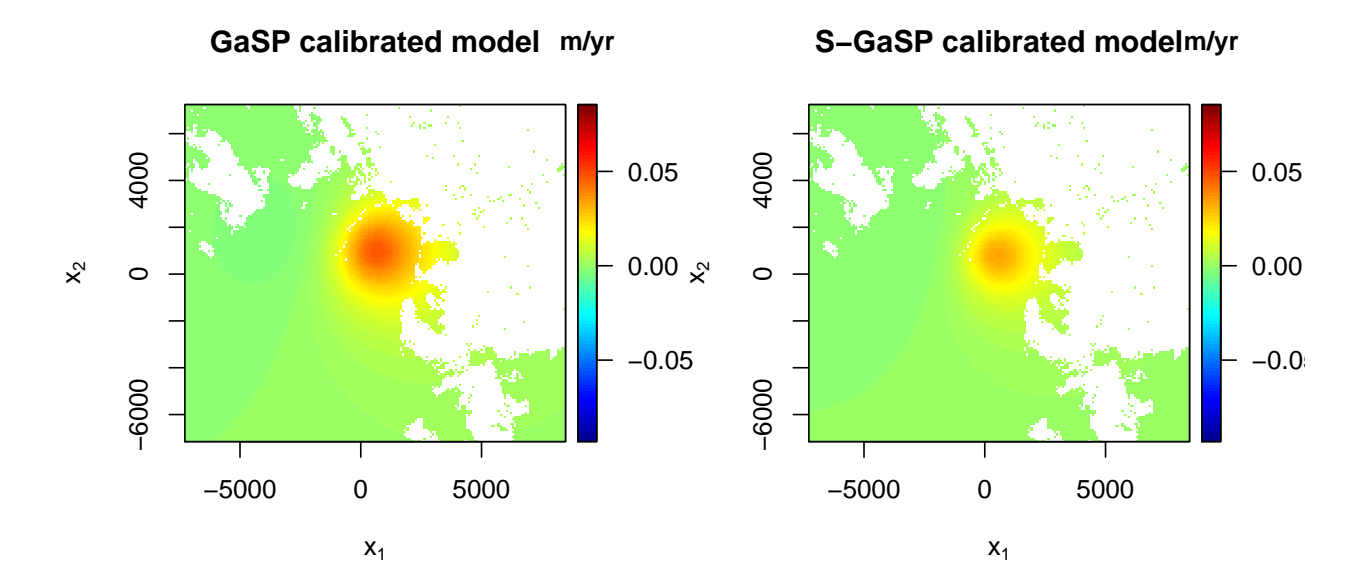


Figure S6: The calibrated geophysical model by the GaSP and S-GaSP are given in the left and right panels.

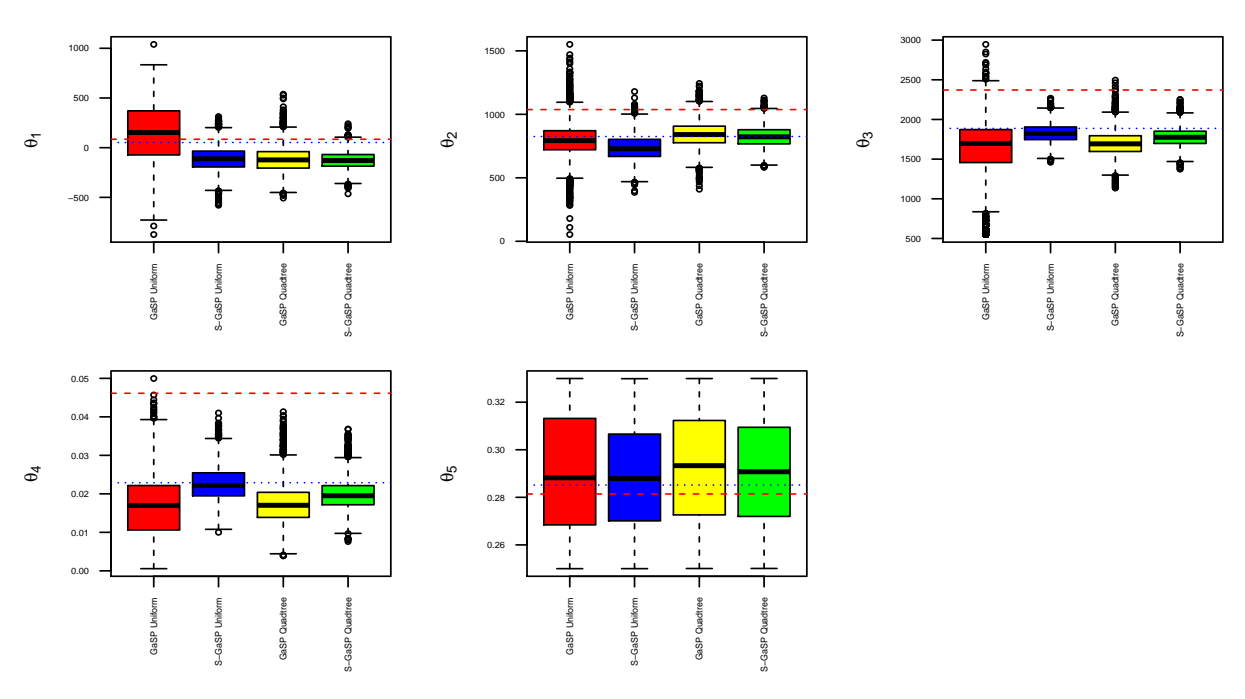


Figure S7: The posterior samples of calibration parameters by image stacking in the GaSP calibration and S-GaSP calibration based on uniform sampling and quadtree sampling of the stack images. The red dashed lines and the blue dotted lines are the posterior mean in the GaSP calibration and S-GaSP calibration based on the five individual images, respectively.

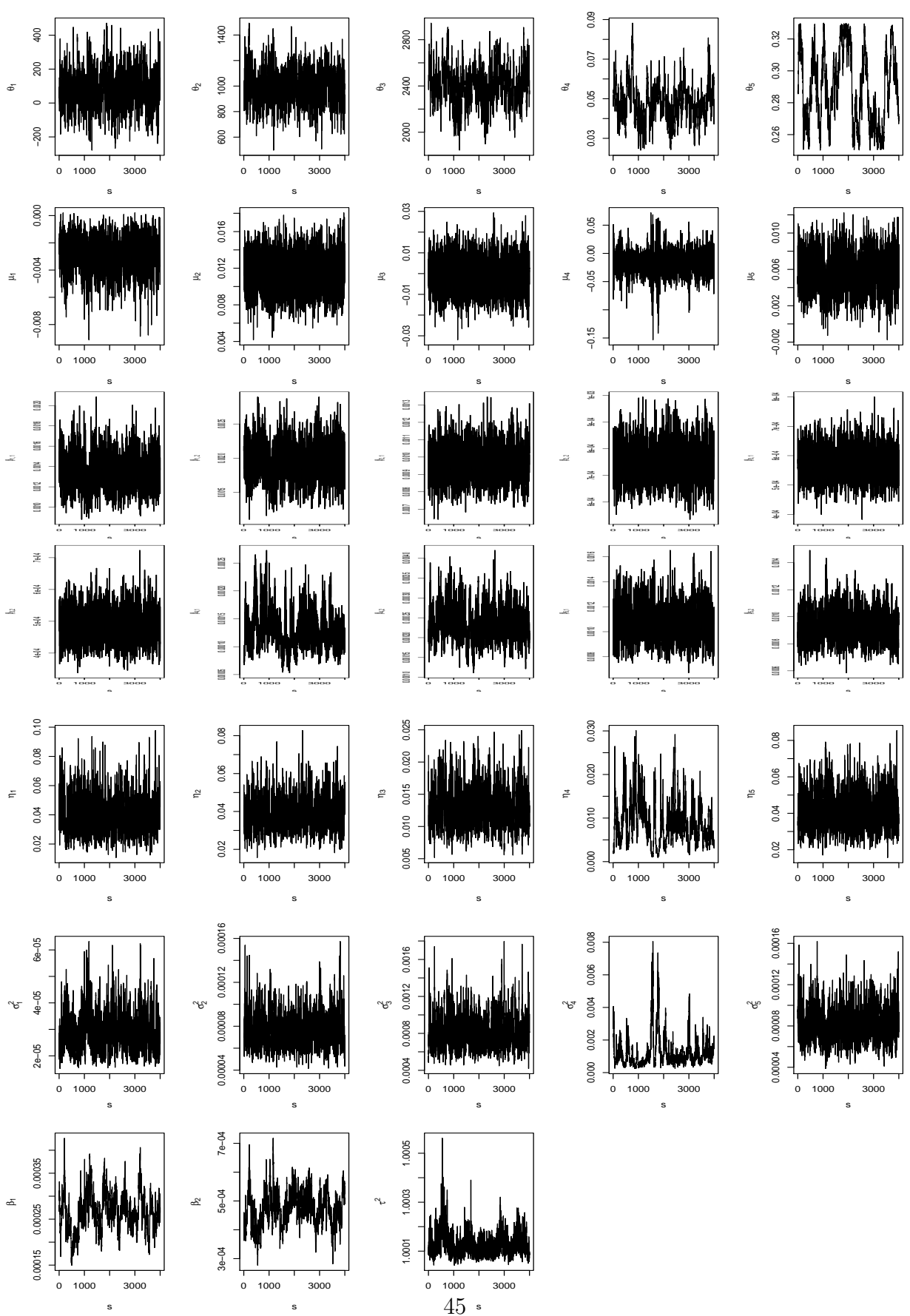


Figure S8: The trace plots of the parameters in the GaSP calibration.

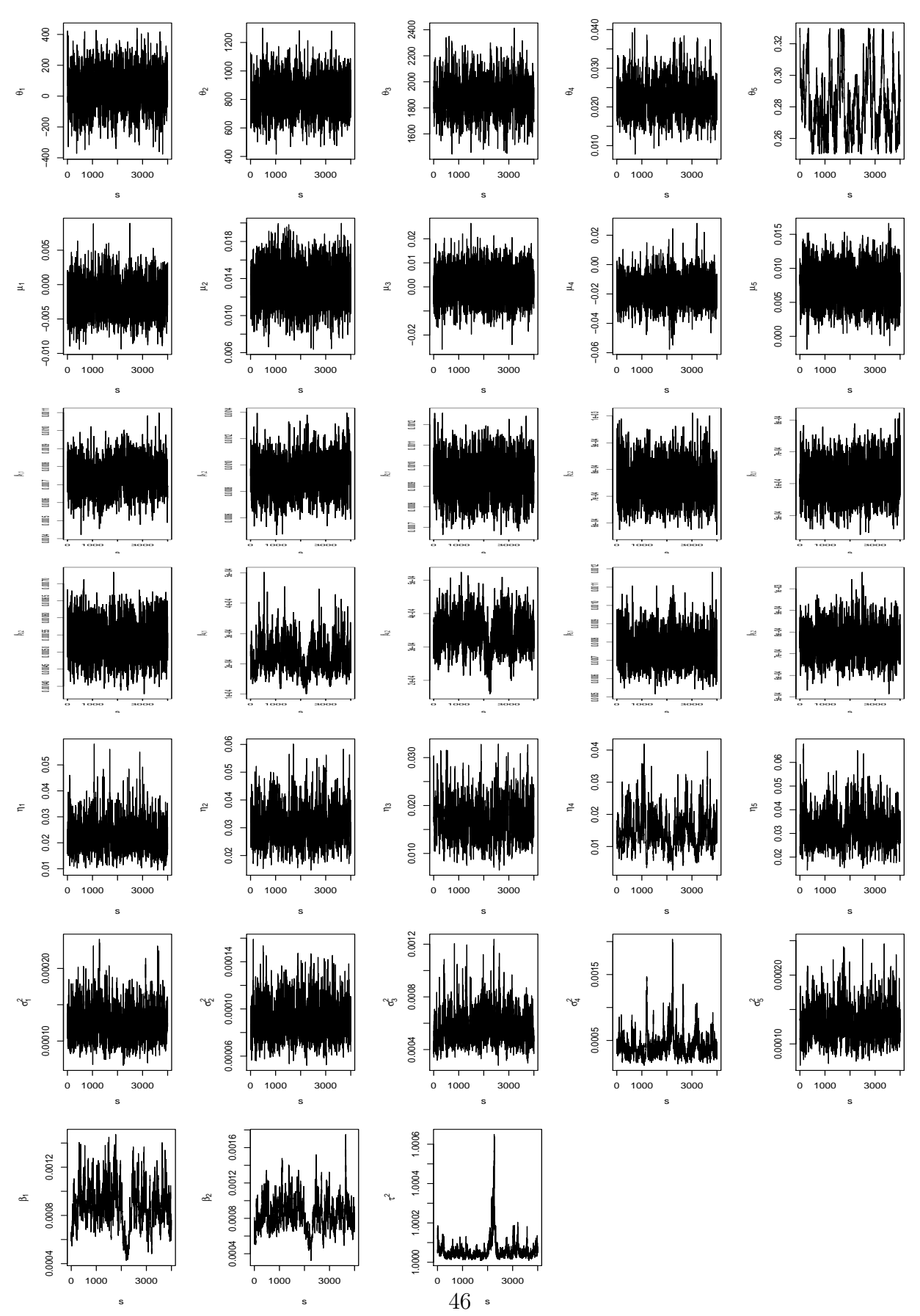


Figure S9: The trace plots of the parameters in the S-GaSP calibration.